

EXPLORATION OF INTERFACIAL THERMAL CONDUCTANCE OF GOLD
NANOPARTICLES USING MOLECULAR DYNAMICS

A Dissertation

Submitted to the Graduate School
of the University of Notre Dame
in Partial Fulfillment of the Requirements
for the Degree of
Doctor of Philosophy

by

Suzanne M. Neidhart,

J. Daniel Gezelter, Director

Graduate Program in Chemistry and Biochemistry
Notre Dame, Indiana
January 2018

© Copyright by
Suzanne M. Neidhart
2017
All Rights Reserved

EXPLORATION OF INTERFACIAL THERMAL CONDUCTANCE OF GOLD
NANOPARTICLES USING MOLECULAR DYNAMICS

Abstract

by

Suzanne M. Neidhart

CONTENTS

FIGURES	iii
TABLES	vi
0.1 Introduction	1
0.1.1 Structures of Self-Assembled Monolayers on Nanoparticles	4
0.2 Computational Details	5
0.2.1 Creating a thermal flux between particles and solvent	5
0.2.2 Interfacial Thermal Conductance	7
0.2.3 Force Fields	8
0.2.4 Simulation Protocol	9
0.3 Results	13
0.3.1 Corrugation of the Particle Surface	15
0.3.2 Orientation of Ligand Chains	19
0.3.3 Orientation of Interfacial Solvent	22
0.3.4 Solvent Penetration of Ligand Layer	23
0.3.5 Ligand-mediated Vibrational Overlap	26
0.4 Discussion	29
0.5 Introduction	32
0.5.0.1 Size- and temperature-dependent particle morphologies .	34
0.5.0.2 Theory	35
0.6 Computational Details	37
0.6.1 Force Fields	38
0.6.2 Simulation Protocol	38
0.7 Results and Discussion	40
0.7.1 Surface Atom Undercoordination	42
0.7.2 Phonon Spectra	46
0.7.3 A Simple Model for Bare Nanoparticle Conductance	50
0.8 Conclusions	51

FIGURES

7	The two extreme cases of ligand orientation relative to the nanoparticle surface: the ligand completely outstretched ($\cos(\theta) = -1$) and the ligand fully lying down on the particle surface ($\cos(\theta) = 0$).	21
8	Computed ligand and interfacial solvent orientational P_2 values for 4 sizes of solvated nanoparticles that are bare or protected with a 50% coverage of C ₄ , C ₈ , or C ₁₂ alkanethiolate ligands. Increasing stiffness of the ligand orients these molecules normal to the particle surface, while the length of the ligand chains works to prevent solvent from lying flat on the surface.	24
9	Radial density profiles for 25 Å radius nanoparticles with no ligands (circles), C ₄ ligands (squares), C ₈ ligands (diamonds), and C ₁₂ ligands (triangles). Ligand density is indicated with filled symbols, solvent (hexane) density is indicated with open symbols. As ligand chain length increases, the nearby solvent is excluded from the ligand layer. The conjugated ligands (upper panel) can create a separated solvent shell within the ligand layer and also allow significantly more solvent to penetrate close to the particle.	25
10	Density overlap parameters (O_{l-s}) for solvated nanoparticles protected by thiolate ligands. In general, the rigidity of the fully-conjugated ligands provides the easiest route for solvent to enter the interfacial region. Additionally, shorter chains allow a greater degree of solvent penetration of the ligand layer.	27
11	The low frequency portion of the vibrational density of states for three chemical components (gold nanoparticles, C ₁₂ ligands, and hexane solvent). These densities of states were computed using the velocity autocorrelation functions for atoms in the interfacial region, constructed with velocities projected onto a direction normal to the interface.	30
12	Interfacial thermal conductance, G , for bare gold nanospheres, cuboctahedra, and icosahedra in contact with hexane solvent. Conductances for flat Au(111), Au(100), and Au(110) interfaces are indicated with dashed horizontal lines. A fit using the model of Tascini <i>et al.</i> is shown along with the predicted value of $G(\infty)$, the infinite particle limit.	41

13	The coordination number of surface atoms as a function of particle size. Filled data points are sampled from simulations, while the dashed lines correspond to ideal icosahedral and cuboctahedral solids. In the spherical case, the large radius limits are shown with open symbols. The large radius limit for the spheres approaches a constant density for all undercoordinated sites, while for the icosahedra, the 9-coordinated (111) facet dominates. In larger cuboctahedra, the relative fraction of 8- and 9-coordinated surface atoms is largely independent of particle size.	45
14	The projected vibrational density of states (Eq. 19) for individual layers in the largest gold nanoparticles (top: spheres, middle: icosahedra, bottom: cuboctahedra). In all systems, the surface layer (green) is significantly enhanced at low frequencies and is shifted down by $\sim 20 \text{ cm}^{-1}$. The Au (bulk) curve shown for comparison is from a perfect FCC lattice in periodic boundary conditions.	48
15	The projected vibrational density of states for all gold atoms (top panel) shows that the phonons in FCC-like nanoparticles (spheres, cuboctahedra) have similar frequency representation, while the non-FCC structures (icosahedra) have significantly altered “bulk” spectra. For surface atoms (bottom panel), the differences in surface undercoordination appear at higher frequencies. These spectra were computed for the largest particles in each of the different morphologies.	49
16	Structurally-predicted thermal conductance values from Eq. (22) compared with the simulated thermal conductance values. Error bars indicate the standard error computed using five replica simulations.	51

TABLES

1	The density of undercoordinated gold atoms at the surface of a facet.	43
---	---	----

Gold Nanospheres

Molecular dynamics simulations of thiolate-protected and solvated gold nanoparticles were carried out in the presence of a non-equilibrium heat flux between the solvent and the core of the particle. The interfacial thermal conductance (G) was computed for these interfaces, and the behavior of the thermal conductance was studied as a function of particle size, ligand flexibility, and ligand chain length. In all cases, thermal conductance of the ligand-protected particles was higher than the bare metal–solvent interface. A number of mechanisms for the enhanced conductance were investigated, including thiolate-driven corrugation of the metal surface, solvent ordering at the interface, solvent-ligand interpenetration, and ligand ordering relative to the particle surface. Only the smallest particles exhibited significant corrugation. All ligands permitted substantial solvent-ligand interpenetration, and ligand chain length has a significant influence on the orientational ordering of interfacial solvent. Solvent – ligand vibrational overlap, particularly in the low frequency range ($< 80\text{cm}^{-1}$) was significantly altered by ligand rigidity, and had direct influence on the interfacial thermal conductance.

Heat transport across various nanostructured interfaces has been the subject of intense experimental interest,[?] [?] [?] [?] [?] [?] [?] [?] and the interfacial thermal conductance, G , is the principal quantity of interest for understanding interfacial heat transport.[?] Because nanoparticles have a significant fraction of their atoms at the particle / solvent interface, the chemical details of these interfaces govern the thermal transport properties. Time-domain thermoreflectance (TDTR) measurements on planar self-assembled monolayer (SAM) junctions between quartz and gold films showed that surface chemistry, particularly the density of covalent bonds to the gold surface, can control energy transport between the two solids.[?]

Experiments and simulations on three-dimensional nanocrystal arrays have similarly shown that surface-attached ligands mediate the thermal transport in these materials, placing particular importance on the overlap between the ligand and nanoparticle vibrational densities of states.[?] Likewise, simulations of polymer-coated gold nanoparticles in water have shown that the surface coating introduces a dominant thermal transport channel to the surrounding solvent.[?]

For ligand-protected nanoparticles in a solvent, there may be three distinct heat transfer processes: (1) from the particles to the ligands, (2) vibrational energy transfer along the length of the ligand, followed by (3) heat transport from the ligand to the surrounding solvent.[?]

Heat transport at the gold-alkylthiolate-solvent interface has been previously explored both through molecular dynamics simulations and via TDTR.[?] Most of these studies have found that alkylthiolates enhance the thermal conductance to the solvent, and that the vibrational overlap provided by the chemically-bound ligand species plays a role in this enhancement.

Reverse nonequilibrium molecular dynamics (RNEMD) methods[?] have been previously applied to calculate the thermal conductance at flat (111) metal / organic solvent interfaces that had been chemically protected by varying coverages of alkanethiolate groups.[?] These simulations suggested an explanation for the increased thermal conductivity at alkanethiol-capped metal surfaces compared with bare metal interfaces. Specifically, the chemical bond between the metal and the ligand introduces a vibrational overlap that is not present without the protecting group, and the overlap between the vibrational spectra (metal to ligand, ligand to solvent) provides a mechanism for rapid thermal transport across the interface. The simulations also suggested that this phenomenon is a non-monotonic func-

tion of the fractional coverage of the surface, as moderate coverages allow energy transfer to solvent molecules that come into close contact with the ligands.

Similarly, simulations of *mixed-chain* alkylthiolate surfaces showed that solvent trapped close to the interface can be efficient at moving thermal energy away from the surface.[?] Trapped solvent molecules that were orientationally aligned with nearby ligands were able to increase the thermal conductance of the interface. This indicates that the ligand-to-solvent vibrational energy transfer is a key feature for increasing particle-to-solvent thermal conductance.

Recently, we extended RNEMD methods for use in non-periodic geometries by creating scaling/shearing moves between concentric regions of a simulation.[?] In this work, we apply this non-periodic variant of RNEMD to investigate the role that *curved* nanoparticle surfaces play in heat and mass transport. On planar surfaces, we discovered that orientational ordering of surface protecting ligands had a large effect on the heat conduction from the metal to the solvent. Smaller nanoparticles have high surface curvature that creates gaps in well-ordered self-assembled monolayers, and the effect of those gaps on the thermal conductance is unknown.

0.0.1 Interfacial Thermal Conductance of Metallic Nanoparticles

For a solvated nanoparticle, it is possible to define a critical value for the interfacial thermal conductance,

$$G_c = \frac{3C_s\Lambda_s}{RC_p} \quad (1)$$

which depends on the solvent heat capacity, C_s , solvent thermal conductivity, Λ_s , particle radius, R , and nanoparticle heat capacity, C_p .[?] In the limit of

infinite interfacial thermal conductance, $G \gg G_c$, cooling of the nanoparticle is limited by the solvent properties, C_s and Λ_s . In the opposite limit, $G \ll G_c$, the heat dissipation is controlled by the thermal conductance of the particle / fluid interface. It is this regime with which we are concerned, where properties of ligands and the particle surface may be tuned to manipulate the rate of cooling for solvated nanoparticles. Based on estimates of G from previous simulations as well as experimental results for solvated nanostructures, gold nanoparticles solvated in hexane are in the $G \ll G_c$ regime for radii smaller than 40 nm. The particles included in this study are more than an order of magnitude smaller than this critical radius, so the heat dissipation should be controlled entirely by the surface features of the particle / ligand / solvent interface.

0.0.1.1 Structures of Self-Assembled Monolayers on Nanoparticles

Though the ligand packing on planar surfaces has been characterized for many different ligands and surface facets, it is not obvious *a priori* how the same ligands will behave on the highly curved surfaces of spherical nanoparticles. Thus, as new applications of ligand-stabilized nanostructures have been proposed, the structure and dynamics of ligands on metallic nanoparticles have been studied using molecular simulation,[?] NMR, XPS, FTIR, calorimetry, and surface microscopies.^{?, ?, ?, ?} Badia, *et al.* used transmission electron microscopy to determine that alkanethiol ligands on gold nanoparticles pack approximately 30% more densely than on planar Au(111) surfaces.[?] Subsequent experiments demonstrated that even at full coverages, surface curvature creates voids between linear ligand chains that can be filled via interdigitation of ligands on neighboring particles.[?] The molecular dynamics simulations of Henz, *et al.* indicate that at low coverages, the

thiolate alkane chains will lie flat on the nanoparticle surface? Above 90% coverage, the ligands stand upright and recover the rigidity and tilt angle displayed on planar facets. Their simulations also indicate a high degree of mixing between the thiolate sulfur atoms and surface gold atoms at high coverages.

In this work, thiolated gold nanospheres were modeled using a united atom force field and non-equilibrium molecular dynamics. Gold nanoparticles with radii ranging from 10 - 25 Å were created from a bulk fcc lattice. These particles were passivated with a 50% coverage (compared with the coverage densities reported by Badia *et al.*) of a selection of thiolates. Three straight-chain thiolates of varying chain lengths and rigidities were utilized. These are summarized in Fig. 1. The passivated particles were then solvated in hexane. Details on the united atom force field are given below and in the supporting information.

0.0.2 Computational Details

0.0.2.1 Creating a thermal flux between particles and solvent

The non-periodic variant of the velocity shearing and scaling RNEMD algorithm (VSS-RNEMD)[?] applies a series of velocity scaling and shearing moves at regular intervals to impose a flux between two concentric spherical regions. To impose a thermal flux between the shells (without an accompanying angular shear), we solve for scaling coefficients a and b ,

$$a = \sqrt{1 - \frac{q_r \Delta t}{K_a - K_a^{\text{rot}}}} \quad (2)$$

$$b = \sqrt{1 + \frac{q_r \Delta t}{K_b - K_b^{\text{rot}}}} \quad (3)$$

Species	Structure
alkanethiolates $n = 4, 8, 12$	
penultimate alkenethiolates $n = 4, 8, 12$	
conjugated alkenethiolates $n = 4$	
$n = 8, 12$	
hexane	

Figure 1. Topologies of the thiolate capping agents and solvent utilized in the simulations. The chemically-distinct sites (S, CH₂, CH₃, CHe, CHa and CH₂a) are treated as united atoms. Most parameters are taken from references ?, ?, ?. Cross-interactions with the Au atoms were adapted from references ?, ?, and ?.

at each time interval. These scaling coefficients conserve total kinetic energy and angular momentum subject to an imposed heat rate, q_r . The coefficients also depend on the instantaneous kinetic energy, $K_{\{a,b\}}$, and the total rotational kinetic energy of each shell, $K_{\{a,b\}}^{\text{rot}} = \sum_i m_i (\mathbf{v}_i \times \mathbf{r}_i)^2 / 2$.

The scaling coefficients are determined and the velocity changes are applied at regular intervals,

$$\mathbf{v}_i \leftarrow a (\mathbf{v}_i - \langle \omega_a \rangle \times \mathbf{r}_i) + \langle \omega_a \rangle \times \mathbf{r}_i \quad (4)$$

$$\mathbf{v}_j \leftarrow b (\mathbf{v}_j - \langle \omega_b \rangle \times \mathbf{r}_j) + \langle \omega_b \rangle \times \mathbf{r}_j. \quad (5)$$

Here $\langle \omega_a \rangle \times \mathbf{r}_i$ is the contribution to the velocity of particle i due to the overall angular velocity of the a shell. In the absence of an angular momentum flux, the angular velocity $\langle \omega_a \rangle$ of the shell is nearly 0 and the resultant particle velocity is a nearly linear scaling of the initial velocity by the coefficient a or b .

Repeated application of this thermal energy exchange yields a radial temperature profile for the solvated nanoparticles that depends linearly on the applied heat rate, q_r . Similar to the behavior in the slab geometries, the temperature profiles have discontinuities at the interfaces between dissimilar materials. The size of the discontinuity depends on the interfacial thermal conductance, which is the primary quantity of interest.

0.0.2.2 Interfacial Thermal Conductance

As described in earlier work,[?] the thermal conductance of each spherical shell may be defined as the inverse Kapitza resistance of the shell. To describe the thermal conductance of an interface of considerable thickness – such as the ligand layers shown here – we can sum the individual thermal resistances of each

concentric spherical shell to arrive at the inverse of the total interfacial thermal conductance. In slab geometries, the intermediate temperatures cancel, but for concentric spherical shells, the intermediate temperatures and surface areas remain in the final sum, requiring the use of a series of individual resistance terms:

$$\frac{1}{G} = R_{\text{total}} = \frac{1}{q_r} \sum_i (T_{i+1} - T_i) 4\pi r_i^2. \quad (6)$$

The longest ligand considered here is in excess of 15 Å in length, and we use 10 concentric spherical shells to describe the total interfacial thermal conductance of the ligand layer.

0.0.2.3 Force Fields

Throughout this work, gold – gold interactions are described by the quantum Sutton-Chen (QSC) model.[?] Previous work[?] has demonstrated that the electronic contributions to heat conduction (which are missing from the QSC model) across heterogeneous metal / non-metal interfaces are negligible compared to phonon excitation, which is captured by the classical model. The hexane solvent is described by the TraPPE united atom model,[?] where sites are located at the carbon centers for alkyl groups. The TraPPE-UA model for hexane provides both computational efficiency and reasonable accuracy for bulk thermal conductivity values. Bonding interactions were used for intra-molecular sites closer than 3 bonds. Effective Lennard-Jones potentials were used for non-bonded interactions.

The TraPPE-UA force field includes parameters for thiol molecules[?] as well as unsaturated and aromatic carbon sites.[?] These were used for the thiolate molecules in our simulations, and missing parameters for the ligands were supplemented using fits described in the supporting information. Bonds are rigid

in TraPPE-UA, so although equilibrium bond distances were taken from this force field, flexible bonds were implemented using bond stretching spring constants adapted from the OPLS-AA force field.[?]

To derive suitable parameters for the thiolates adsorbed on Au(111) surfaces, we adopted the S parameters from Luedtke and Landman[?] and modified the parameters for the CTS atom to maintain charge neutrality in the molecule.

Other interactions between metal (Au) and non-metal atoms were adapted from an adsorption study of alkyl thiols on gold surfaces by Vlugt, *et al.*[?] They fit an effective pair-wise Lennard-Jones form of potential parameters for the interaction between Au and pseudo-atoms CH_x and S based on a well-established and widely-used effective potential of Hautman and Klein for the Au(111) surface.[?]

All additional terms to represent thiolated alkenes and conjugated ligand moieties were parameterized as part of this work and are available in the supporting information. All simulations were carried out with the open source molecular dynamics package, OpenMD.[? ?]

0.0.2.4 Simulation Protocol

Gold nanospheres with radii ranging from 10 - 25 Å were created from a bulk fcc lattice and were thermally equilibrated prior to the addition of ligands. A 50% coverage of ligands (based on coverages reported by Badia, *et al.*[?]) was placed on the surface of the equilibrated nanoparticles using Packmol[?]. We have chosen three lengths for the straight-chain ligands, C_4 , C_8 , and C_{12} , differentiated by the number of carbons in the chains. Additionally, to explore the effects of ligand flexibility, we have used three levels of ligand “stiffness”. The most flexible chain is a fully saturated alkanethiolate, while moderate rigidity is introduced using an

alkene thiolate with one double bond in the penultimate (solvent-facing) carbon-carbon location. The most rigid ligands are fully-conjugated chains where all of the carbons are represented with conjugated (aryl) united-atom carbon atoms (CH_{ar} or terminal CH₂ar).

The nanoparticle / ligand complexes were thermally equilibrated to allow for ligand conformational flexibility. Packmol was then used to solvate the structures inside a spherical droplet of hexane. The thickness of the solvent layer was chosen to be at least 1.5× the combined radius of the nanoparticle / ligand structure. The fully solvated system was equilibrated for at least 1 ns using the “Langevin Hull” algorithm to apply 50 atm of pressure and a target temperature of 250 K.[?] [] Typical system sizes ranged from 18,310 united atom sites for the 10 Å particles with C_4 ligands to 89,490 sites for the 25 Å particles with C_{12} ligands. Figure 2 shows one of the solvated 25 Å nanoparticles passivated with the C_{12} alkane thiolate ligands.

Once equilibrated, thermal fluxes were applied for 1 ns, until stable temperature gradients had developed (see figure 3). Systems were run under moderate pressure (50 atm) with an average temperature (250K) that maintained a compact solvent cluster and avoided formation of a vapor layer near the heated metal surface. Pressure was applied to the system via the non-periodic “Langevin Hull” algorithm.[?] [] However, thermal coupling to the external temperature bath was removed to avoid interference with the imposed RNEMD flux.

Although the VSS-RNEMD moves conserve *total* angular momentum and energy, systems which contain a metal nanoparticle embedded in a significant volume of solvent will still experience nanoparticle diffusion inside the solvent droplet. To aid in measuring an accurate temperature profile for these systems, a single gold

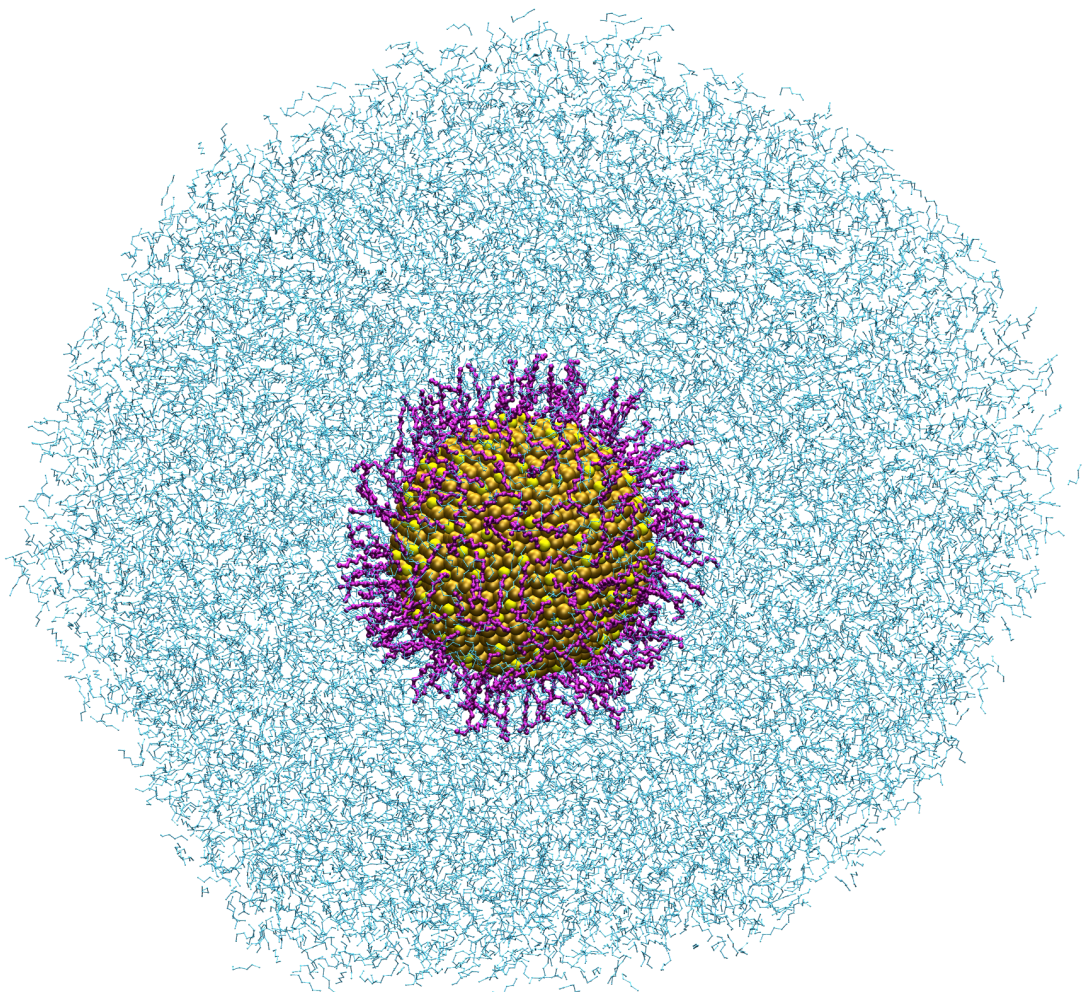


Figure 2. A 25 Å radius gold nanoparticle protected with a half-monolayer of TraPPE-UA dodecanethiolate (C_{12}) ligands and solvated in TraPPE-UA hexane. The interfacial thermal conductance is computed by applying a kinetic energy flux between the nanoparticle and an outer shell of solvent.

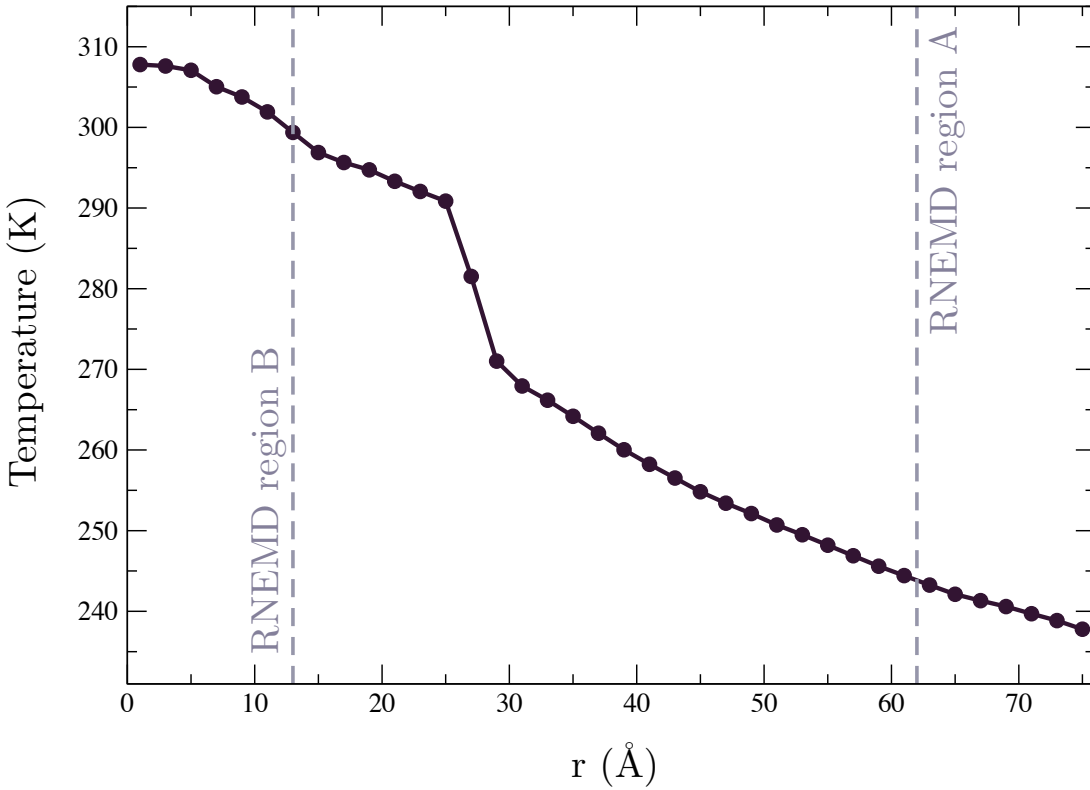


Figure 3. Radial temperature profile for a 25 Å radius particle protected with a 50% coverage of TraPPE-UA butanethiolate (C_4) ligands and solvated in TraPPE-UA hexane. A kinetic energy flux is applied between RNEMD region A and RNEMD region B. The size of the temperature discontinuity at the interface is governed by the interfacial thermal conductance.

atom at the origin of the coordinate system was assigned a mass $10,000 \times$ its original mass. The bonded and nonbonded interactions for this atom remain unchanged and the heavy atom is excluded from the RNEMD velocity scaling. The only effect of this gold atom is to effectively pin the nanoparticle at the origin of the coordinate system, thereby preventing translational diffusion of the nanoparticle due to Brownian motion.

To provide statistical independence, five separate configurations were simulated for each particle radius and ligand. The structures were unique, starting at the point of ligand placement, in order to sample multiple surface-ligand configurations.

0.0.3 Results

We modeled four sizes of nanoparticles ($R = 10, 15, 20,$ and 25 \AA). The smallest particle size produces the lowest interfacial thermal conductance values for most of the protecting groups (Fig. 4). Between the other three sizes of nanoparticles, there is no systematic dependence of the interfacial thermal conductance on the nanoparticle size. It is likely that the differences in local curvature of the nanoparticle sizes studied here do not disrupt the ligand packing and behavior in drastically different ways.

Unlike our previous study of varying thiolate ligand chain lengths on planar Au(111) surfaces, the interfacial thermal conductance of ligand-protected nanospheres exhibits a distinct dependence on the ligand identity. A half-monolayer coverage of ligands yields interfacial conductance that is strongly dependent on both ligand length and flexibility.

There are many factors that could be playing a role in the ligand-dependent

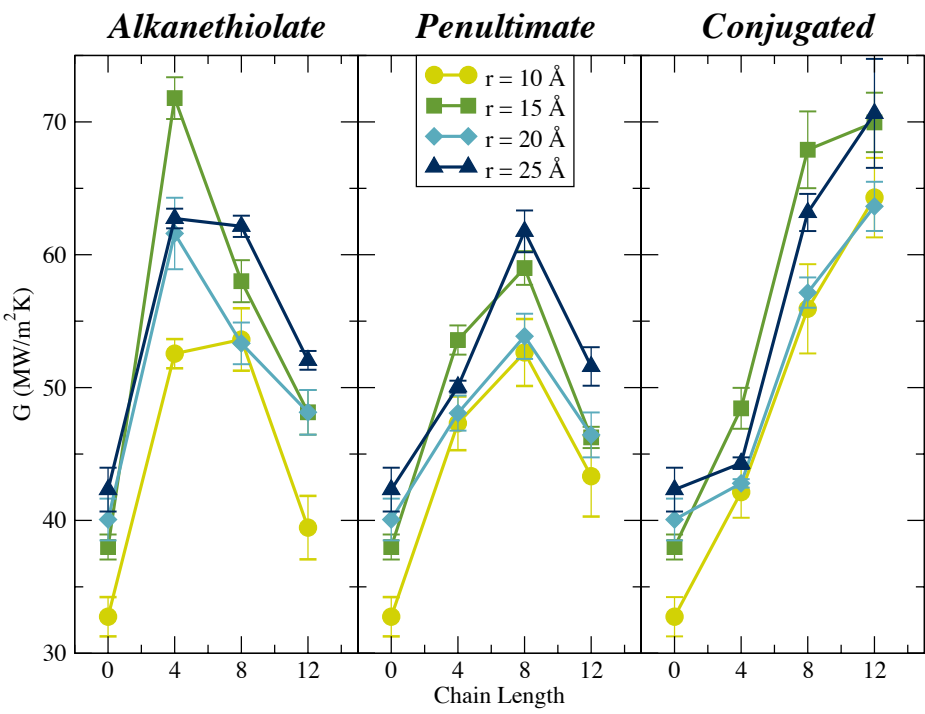


Figure 4. Interfacial thermal conductance (G) values for 4 sizes of solvated nanoparticles that are bare or protected with a 50% coverage of C_4 , C_8 , or C_{12} thiolate ligands. Ligands of different flexibility are shown in separate panels. The middle panel indicates ligands which have a single carbon-carbon double bond in the penultimate position.

conductuance. The sulfur-gold interaction is particularly strong, and the presence of the ligands can easily disrupt the crystalline structure of the gold at the surface of the particles, providing more efficient scattering of phonons into the ligand / solvent layer. This effect would be particularly important at small particle sizes.

In previous studies of mixed-length ligand layers with full coverage, we observed that ligand-solvent alignment was an important factor for heat transfer into the solvent. With high surface curvature and lower effective coverages, ligand behavior also becomes more complex. Some chains may be lying down on the surface, and solvent may not be penetrating the ligand layer to the same degree as in the planar surfaces.

Additionally, the ligand flexibility directly alters the vibrational density of states for the layer that mediates the transfer of phonons between the metal and the solvent. This could be a partial explanation for the observed differences between the fully conjugated and more flexible ligands.

In the following sections we provide details on how we measure surface corrugation, solvent-ligand interpenetration, and ordering of the solvent and ligand at the surfaces of the nanospheres. We also investigate the overlap between vibrational densities of states for the various ligands.

0.0.3.1 Corrugation of the Particle Surface

The bonding sites for thiols on gold surfaces have been studied extensively and include configurations beyond the traditional atop, bridge, and hollow sites found on planar surfaces. In particular, the deep potential well between the gold atoms and the thiolate sulfur atoms leads to insertion of the sulfur into the gold lattice and displacement of interfacial gold atoms. The degree of ligand-induced surface

restructuring may have an impact on the interfacial thermal conductance and is an important phenomenon to quantify.

Henz, *et al.*[?] used the metal density as a function of radius to measure the degree of mixing between the thiol sulfurs and surface gold atoms at the edge of a nanoparticle. Although metal density is important, disruption of the local crystalline ordering would also have a large effect on the phonon spectrum in the particles. To measure this effect, we use the fraction of gold atoms exhibiting local fcc ordering as a function of radius to describe the ligand-induced disruption of the nanoparticle surface.

The local bond orientational order can be described using the method of Steinhardt *et al.*[?] The local bonding environment, $\bar{q}_{\ell m}$, for each atom in the system is determined by averaging over the spherical harmonics between that atom and each of its neighbors,

$$\bar{q}_{\ell m} = \sum_i Y_{\ell}^m(\theta_i, \phi_i) \quad (7)$$

where θ_i and ϕ_i are the relative angular coordinates of neighbor i in the laboratory frame. A global average orientational bond order parameter, $\bar{Q}_{\ell m}$, is the average over each $\bar{q}_{\ell m}$ for all atoms in the system. To remove the dependence on the laboratory coordinate frame, the third order rotationally invariant combination of $\bar{Q}_{\ell m}$, \hat{w}_{ℓ} , is utilized here.[? ?]

For $\ell = 4$, the ideal face-centered cubic (fcc), body-centered cubic (bcc), hexagonally close-packed (hcp), and simple cubic (sc) local structures exhibit \hat{w}_4 values of -0.159, 0.134, 0.159, and 0.159, respectively. Because \hat{w}_4 exhibits an extreme value for fcc structures, it is ideal for measuring local fcc ordering. The spatial distribution of \hat{w}_4 local bond orientational order parameters, $p(\hat{w}_4, r)$, can provide information about the location of individual atoms that are central to local fcc

ordering.

The fraction of fcc-ordered gold atoms at a given radius in the nanoparticle,

$$f_{\text{fcc}}(r) = \int_{-\infty}^{w_c} p(\hat{w}_4, r) d\hat{w}_4 \quad (8)$$

is described by the distribution of the local bond orientational order parameters, $p(\hat{w}_4, r)$, and w_c , a cutoff for the peak \hat{w}_4 value displayed by fcc structures. A w_c value of -0.12 was chosen to isolate the fcc peak in \hat{w}_4 .

As illustrated in Figure 5, the presence of ligands decreases the fcc ordering of the gold atoms at the nanoparticle surface. For the smaller nanoparticles, this disruption extends into the core of the nanoparticle, indicating widespread disruption of the lattice.

We may describe the thickness of the disrupted nanoparticle surface by defining a corrugation factor, c , as the ratio of the radius at which the fraction of gold atoms with fcc ordering is 0.9 and the radius at which the fraction is 0.5.

$$c = 1 - \frac{r(f_{\text{fcc}} = 0.9)}{r(f_{\text{fcc}} = 0.5)} \quad (9)$$

A sharp interface will have a steep drop in f_{fcc} at the edge of the particle ($c \rightarrow 0$). In the opposite limit where the entire nanoparticle surface is restructured by ligands, the radius at which there is a high probability of fcc ordering moves dramatically inward ($c \rightarrow 1$).

The computed corrugation factors are shown in Figure 6 for bare nanoparticles and for ligand-protected particles as a function of ligand chain length. The largest nanoparticles are only slightly restructured by the presence of ligands on the surface, while the smallest particle ($r = 10 \text{ \AA}$) exhibits significant disruption of

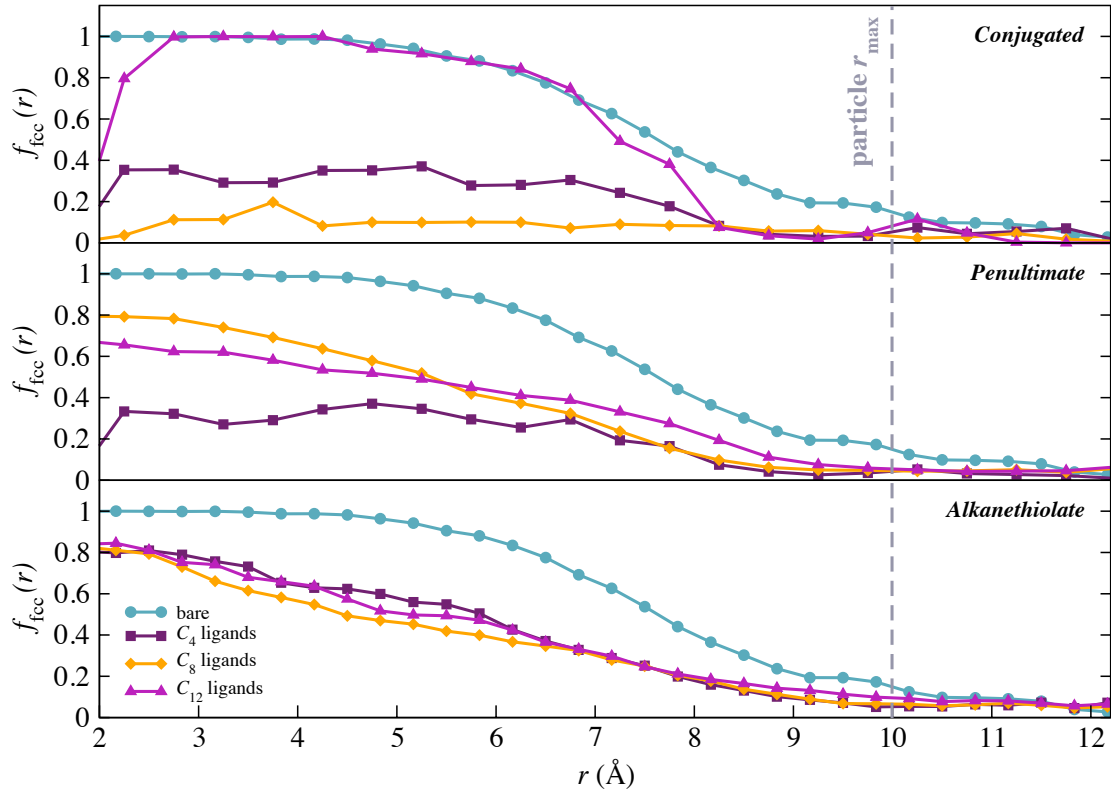


Figure 5. Fraction of gold atoms with fcc ordering as a function of radius for a 10 Å radius nanoparticle. The decreased fraction of fcc-ordered atoms in ligand-protected nanoparticles relative to bare particles indicates restructuring of the nanoparticle surface by the thiolate sulfur atoms.

the original fcc ordering when covered with a half-monolayer of thiol ligands.

Because the thiolate ligands do not significantly alter the larger particle crystallinity, the surface corrugation does not seem to be a likely candidate to explain the large increase in thermal conductance at the interface when ligands are added.

0.0.3.2 Orientation of Ligand Chains

Previous theoretical work on heat conduction through alkane chains has shown that short chains are dominated by harmonic interactions, where the energy is carried ballistically through the chain.[?] As the saturated ligand chain length increases in length, it exhibits significantly more conformational flexibility. Thus, different lengths of ligands should favor different chain orientations on the surface of the nanoparticle, and can localize the ligand vibrational density of states close to the particle, lowering the effectiveness of the heat conduction.[?] To determine the distribution of ligand orientations relative to the particle surface we examine the probability of finding a ligand with a particular orientation relative to the surface normal of the nanoparticle,

$$\cos(\theta) = \frac{\vec{r}_i \cdot \hat{u}_i}{|\vec{r}_i||\hat{u}_i|} \quad (10)$$

where \vec{r}_i is the vector between the cluster center of mass and the sulfur atom on ligand molecule i , and \hat{u}_i is the vector between the sulfur atom and CH₃ pseudo-atom on ligand molecule i . As depicted in Figure 7, $\theta \rightarrow 180^\circ$ for a ligand chain standing upright on the particle ($\cos(\theta) \rightarrow -1$) and $\theta \rightarrow 90^\circ$ for a ligand chain lying down on the surface ($\cos(\theta) \rightarrow 0$). As the thiolate alkane chain increases in length and becomes more flexible, the ligands are more willing to lie down on the nanoparticle surface and exhibit increased population at $\cos(\theta) = 0$.

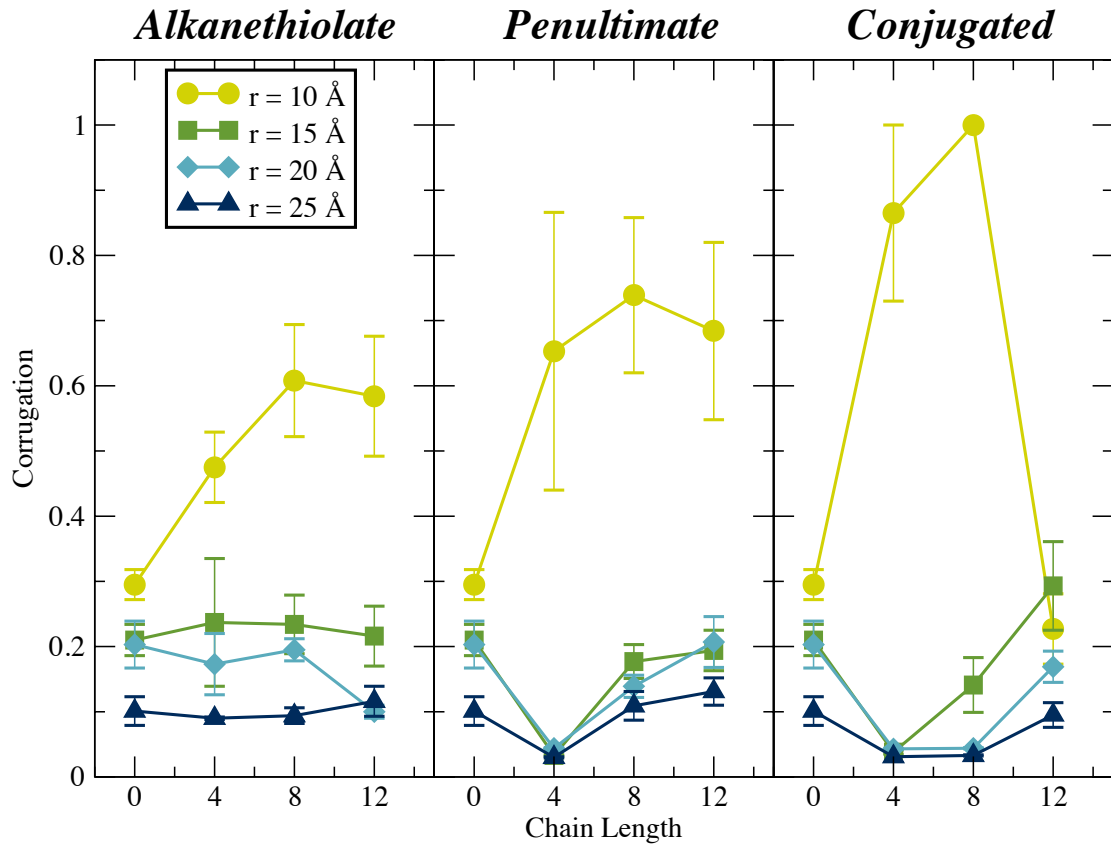


Figure 6. Computed corrugation values for 4 sizes of solvated nanoparticles that are bare or protected with a 50% coverage of C₄, C₈, or C₁₂ thiolate ligands. The smallest (10 Å) particles show significant disruption to their crystal structures, and the length and stiffness of the ligands is a contributing factor to the surface disruption.

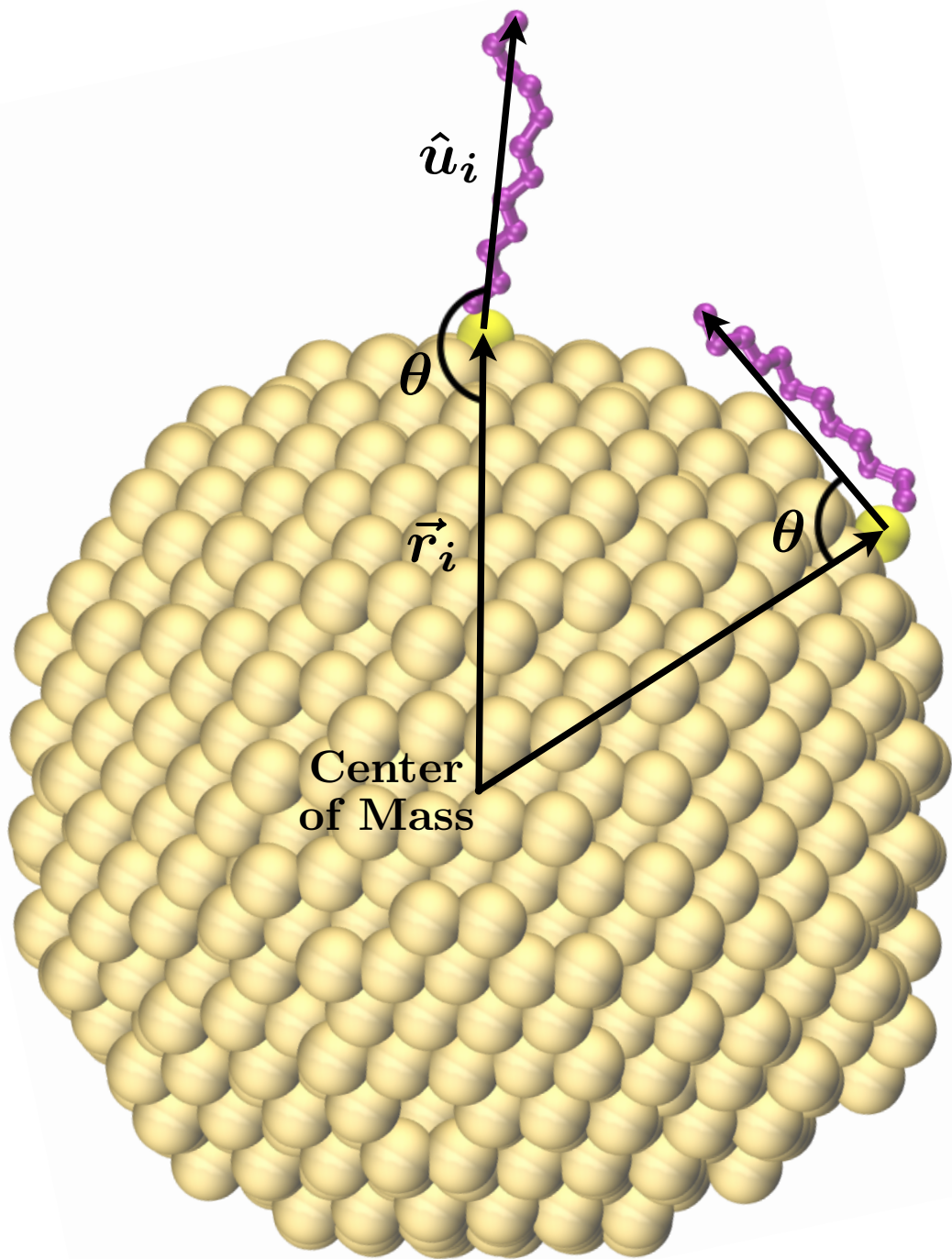


Figure 7. The two extreme cases of ligand orientation relative to the nanoparticle surface: the ligand completely outstretched ($\cos(\theta) = -1$) and the ligand fully lying down on the particle surface ($\cos(\theta) = 0$).

An order parameter describing the average ligand chain orientation relative to the nanoparticle surface is available using the second order Legendre parameter,

$$P_2 = \left\langle \frac{1}{2} (3 \cos^2(\theta) - 1) \right\rangle \quad (11)$$

Ligand populations that are perpendicular to the particle surface have P_2 values of 1, while ligand populations lying flat on the nanoparticle surface have P_2 values of -0.5 . Disordered ligand layers will exhibit mean P_2 values of 0. As shown in Figure 8 the ligand P_2 values approaches 0 as ligand chain length – and ligand flexibility – increases.

0.0.3.3 Orientation of Interfacial Solvent

Similarly, we examined the distribution of *hexane* molecule orientations relative to the particle surface using the same angular analysis utilized for the ligand chain orientations. In this case, \vec{r}_i is the vector between the particle center of mass and one of the CH_2 pseudo-atoms in the middle of hexane molecule i and \hat{u}_i is the vector between the two CH_3 pseudo-atoms on molecule i . Since we are only interested in the orientation of solvent molecules near the ligand layer, we select only the hexane molecules within a specific r -range, between the edge of the particle and the end of the ligand chains. A large population of hexane molecules with $\cos(\theta) \sim \pm 1$ would indicate interdigitation of the solvent molecules between the upright ligand chains. A more random distribution of $\cos(\theta)$ values indicates a disordered arrangement of solvent molecules near the particle surface. Again, P_2 order parameter values provide a population analysis for the solvent that is close to the particle surface.

The average orientation of the interfacial solvent molecules is notably flat on

the *bare* nanoparticle surfaces. This blanket of hexane molecules on the particle surface may act as an insulating layer, increasing the interfacial thermal resistance. As the length (and flexibility) of the ligand increases, the average interfacial solvent P_2 value approaches 0, indicating a more random orientation of the ligand chains. The average orientation of solvent within the C_8 and C_{12} ligand layers is essentially random. Solvent molecules in the interfacial region of C_4 ligand-protected nanoparticles do not lie as flat on the surface as in the case of the bare particles, but are not as randomly oriented as the longer ligand lengths.

These results are particularly interesting in light of our previous results[?], where solvent molecules readily filled the vertical gaps between neighboring ligand chains and there was a strong correlation between ligand and solvent molecular orientations. It appears that the introduction of surface curvature and a lower ligand packing density creates a disordered ligand layer that lacks well-formed channels for the solvent molecules to occupy.

0.0.3.4 Solvent Penetration of Ligand Layer

The extent of ligand – solvent interaction is also determined by the degree to which these components occupy the same region of space adjacent to the nanoparticle. The radial density profiles of these components help determine this degree of interaction. Figure 9 shows representative density profiles for solvated 25 Å radius nanoparticles with no ligands, and with a 50% coverage of C_4 , C_8 , and C_{12} thiolates.

The differences between the radii at which the hexane surrounding the ligand-covered particles reaches bulk density correspond nearly exactly to the differences between the lengths of the ligand chains. Beyond the edge of the ligand layer,

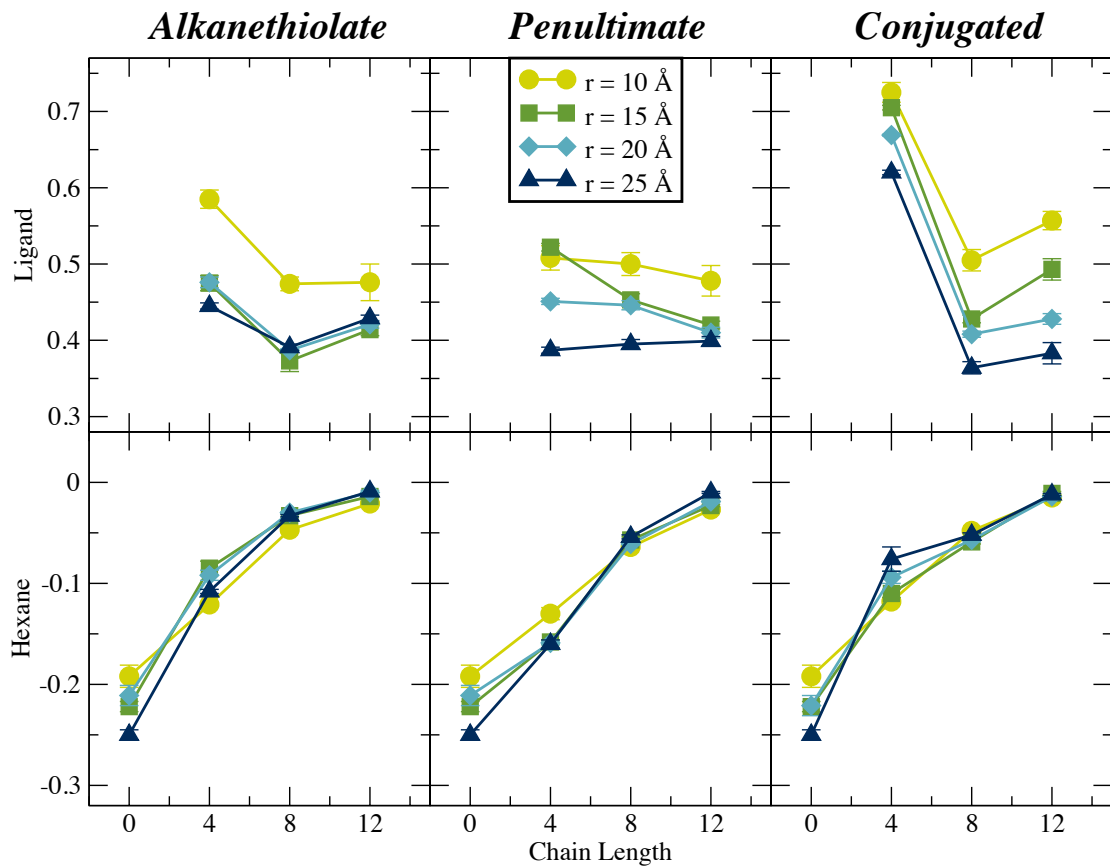


Figure 8. Computed ligand and interfacial solvent orientational P_2 values for 4 sizes of solvated nanoparticles that are bare or protected with a 50% coverage of C₄, C₈, or C₁₂ alkanethiolate ligands. Increasing stiffness of the ligand orients these molecules normal to the particle surface, while the length of the ligand chains works to prevent solvent from lying flat on the surface.

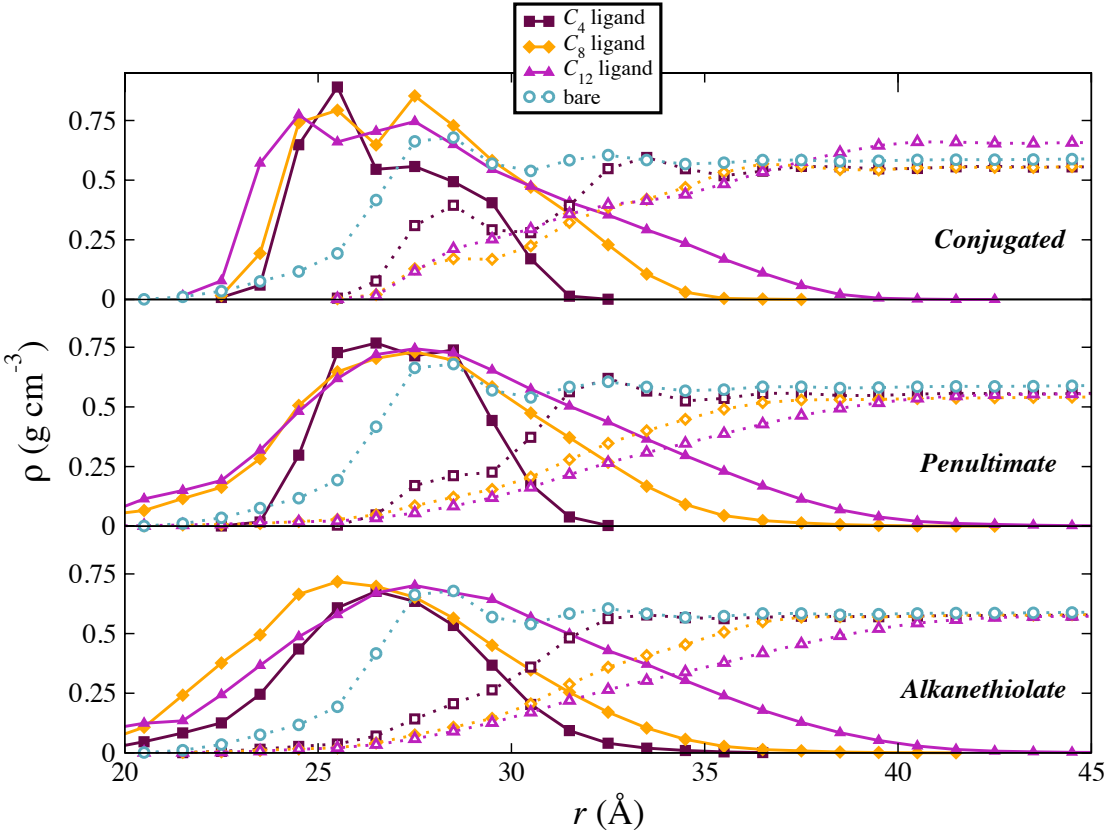


Figure 9. Radial density profiles for 25 Å radius nanoparticles with no ligands (circles), C_4 ligands (squares), C_8 ligands (diamonds), and C_{12} ligands (triangles). Ligand density is indicated with filled symbols, solvent (hexane) density is indicated with open symbols. As ligand chain length increases, the nearby solvent is excluded from the ligand layer. The conjugated ligands (upper panel) can create a separated solvent shell within the ligand layer and also allow significantly more solvent to penetrate close to the particle.

the solvent reaches its bulk density within a few angstroms. The differing shapes of the density curves indicate that the solvent is increasingly excluded from the ligand layer as the chain length increases.

The conjugated ligands create a distinct solvent shell within the ligand layer and also allow significantly more solvent to penetrate close to the particle. We define a density overlap parameter,

$$O_{l-s} = \frac{1}{V} \int_0^{r_{\max}} 4\pi r^2 \frac{4\rho_l(r)\rho_s(r)}{(\rho_l(r) + \rho_s(r))^2} dr \quad (12)$$

where $\rho_l(r)$ and $\rho_s(r)$ are the ligand and solvent densities at a radius r , and V is the total integration volume ($V = 4\pi r_{\max}^3/3$). The fraction in the integrand is a dimensionless quantity that is unity when ligand and solvent densities are identical at radius r , but falls to zero when either of the two components are excluded from that region.

The density overlap parameters are shown in Fig. 10. The calculated overlap parameters indicate that the conjugated ligand allows for the most solvent penetration close to the particle, and that shorter chains generally permit greater solvent penetration in the interfacial region. Increasing overlap can certainly allow for enhanced thermal transport, but this is clearly not the only contributing factor. Even when the solvent and ligand are in close physical contact, there must also be good vibrational overlap between the phonon densities of states in the ligand and solvent to transmit vibrational energy between the two materials.

0.0.3.5 Ligand-mediated Vibrational Overlap

In phonon scattering models for interfacial thermal conductance,[? ? ? ? ?] the frequency-dependent transmission probability ($t_{a \rightarrow b}(\omega)$) predicts phonon

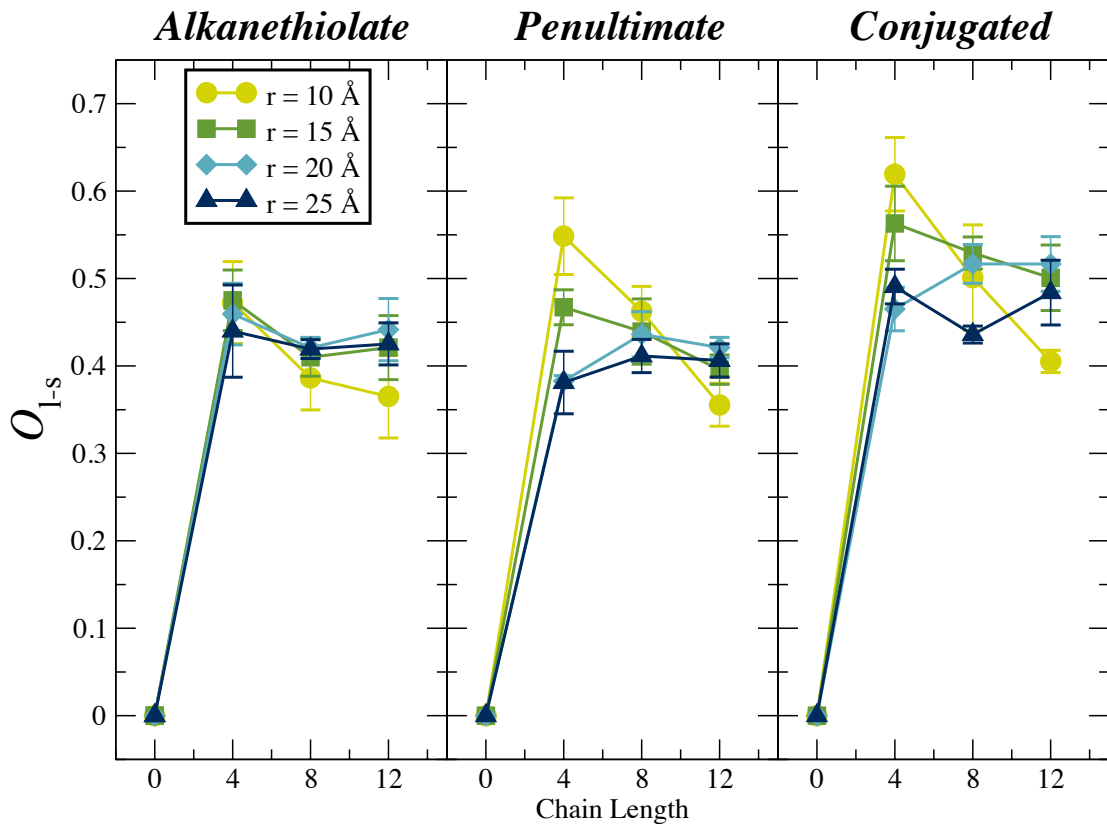


Figure 10. Density overlap parameters (O_{l-s}) for solvated nanoparticles protected by thiolate ligands. In general, the rigidity of the fully-conjugated ligands provides the easiest route for solvent to enter the interfacial region. Additionally, shorter chains allow a greater degree of solvent penetration of the ligand layer.

transfer between materials a and b . Many of the models for interfacial phonon transmission estimate this quantity using the phonon density of states and group velocity, and make use of a Debye model for the density of states in the solid.

A consensus picture is that in order to transfer the energy carried by an incoming phonon of frequency ω on the a side, the phonon density of states on the b side must have a phonon of the same frequency. The overlap of the phonon densities of states, particularly at low frequencies, therefore contributes to the transfer of heat. Phonon scattering must also be done in a direction perpendicular to the interface. In the geometries described here, there are two interfaces (particle → ligand, and ligand → solvent), and the vibrational overlap between the ligand and the other two components is going to be relevant to heat transfer.

To estimate the relevant densities of states, we have projected the velocity of each atom i in the region of the interface onto a direction normal to the interface. For the nanosphere geometries studied here, the normal direction depends on the instantaneous position of the atom relative to the center of mass of the particle.

$$v_{\perp}(t) = \mathbf{v}(t) \cdot \frac{\mathbf{r}(t)}{|\mathbf{r}(t)|} \quad (13)$$

The quantity $v_{\perp}(t)$ measures the instantaneous velocity of an atom in a direction perpendicular to the nanoparticle interface. In the interfacial region, the autocorrelation function of these velocities,

$$C_{\perp}(t) = \langle v_{\perp}(t) \cdot v_{\perp}(0) \rangle, \quad (14)$$

will include contributions from all of the phonon modes present at the interface. The Fourier transform of the time-symmetrized autocorrelation function provides

an estimate of the vibrational density of states,[?]

$$\rho(\omega) = \frac{1}{\tau} \int_{-\tau/2}^{\tau/2} C_{\perp}(t) e^{-i\omega t} dt. \quad (15)$$

Here τ is the total observation time for the autocorrelation function. In Fig. 11 we show the low-frequency region of the normalized vibrational densities of states for the three chemical components (gold nanoparticle, C_{12} ligands, and interfacial solvent). The double bond in the penultimate location is a small perturbation on ligands of this size, and that is reflected in relatively similar spectra in the lower panels. The fully conjugated ligand, however, pushes the peak in the lowest frequency band from $\sim 29\text{cm}^{-1}$ to $\sim 55\text{cm}^{-1}$, yielding significant overlap with the density of states in the nanoparticle. This ligand also increases the overlap with the solvent density of states in a band between 280 and 380 cm^{-1} . This provides some physical basis for the high interfacial conductance observed for the fully conjugated C_8 and C_{12} ligands.

The similarity between the density of states for the alkanethiolate and penultimate ligands also helps explain why the interfacial conductance is nearly the same for these two ligands, particularly at longer chain lengths.

0.0.4 Discussion

The chemical bond between the metal and the ligand introduces vibrational overlap that is not present between the bare metal surface and solvent. Thus, regardless of ligand identity or chain length, the presence of a half-monolayer ligand coverage yields a higher interfacial thermal conductance value than the bare nanoparticle. The mechanism for the varying conductance for the different ligands is somewhat less clear. Ligand-based alterations to vibrational density of

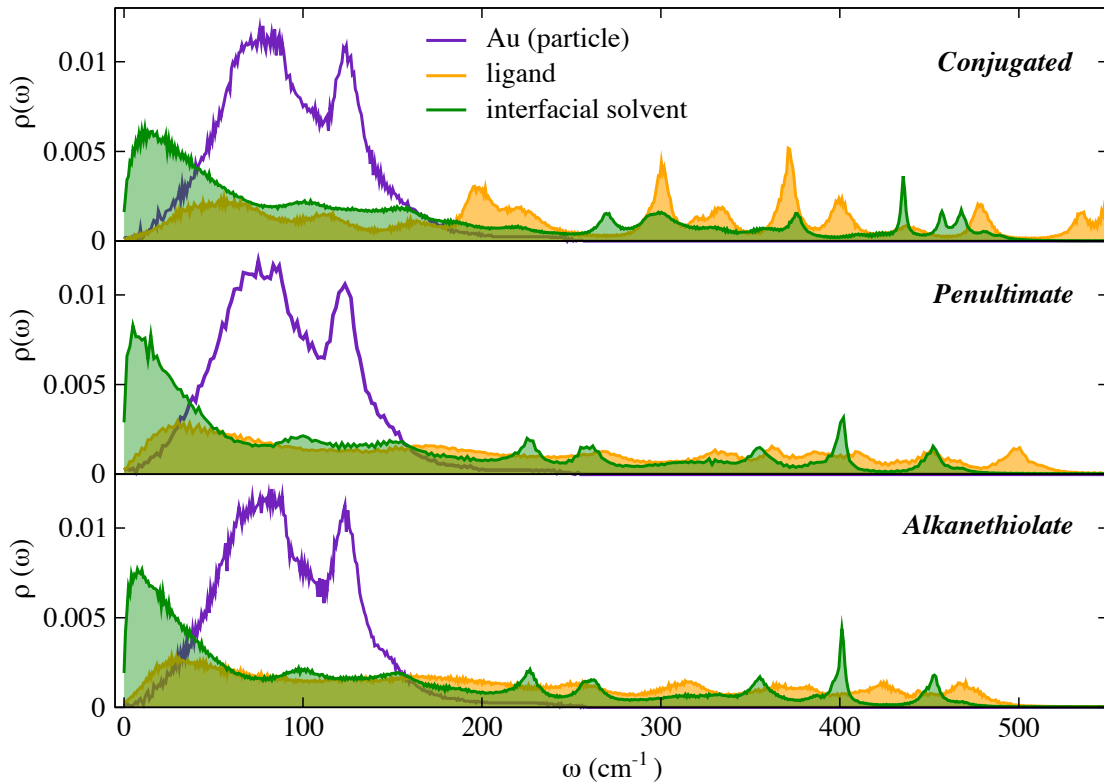


Figure 11. The low frequency portion of the vibrational density of states for three chemical components (gold nanoparticles, C₁₂ ligands, and hexane solvent). These densities of states were computed using the velocity autocorrelation functions for atoms in the interfacial region, constructed with velocities projected onto a direction normal to the interface.

states is a major contributor, but some of the ligands can disrupt the crystalline structure of the smaller nanospheres, while others can re-order the interfacial solvent and alter the interpenetration profile between ligand and solvent chains. Further work to separate the effects of ligand-solvent interpenetration and surface reconstruction is clearly needed for a complete picture of the heat transport in these systems.

Molecular dynamics simulations were performed to model the interfacial thermal conductance (G) from bare gold nanoparticles (icosahedral, cuboctahedral, and spherical) to a hexane solvent. The computed conductance was found to depend not only on particle shape, but also on the size of the nanoparticles, particularly for nanospheres. These results are compared with conductance out of the planar facets: (111), (100), and (110); all commonly exhibited in small patches by the spherical particles. Undercoordination of the surface atoms and the vibrational density of states in the icosahedra explain some of these observations. The exposed surfaces of icosahedral particles are dominated by (111) facets with 9-coordinated gold atoms. Cuboctahedral particles are dominated by the (100) and (111) facets with 8- and 9-coordinated surface atoms, respectively. The nanospheres approach a constant surface density of 6-9 coordinated sites at large particle sizes, and these surface atoms play a large role in the conductance to the solvent. The surface-normal vibrational densities of states were used to explain a simple surface undercoordination model, which shows a size-dependent enhancement of low-frequency coupling to the solvent.

Thermal transport between nanoparticles and their surrounding environments depends on many factors, including particle size,[? ? ? ? ?] composition,[? ? ?] surface modification,[? ? ? ? ? ? ? ? ? ?] surface supports,[? ?] exposed surface facets,[? ? ?] and the chemical details of the environment.[? ? ? ? ? ? ? ? ? ? ? ?] Particle morphology may also play a role in heat transfer out of nanostructures. This is the central question of this work – all other things being equal, will different particle morphologies yield different heat transfer properties to the solvent?

Tascini *et al.*[?] recently studied the curvature dependence of the interfacial

thermal conductance for partially solvated nanospheres. They found an empirical relationship,

$$G(r) = G(\infty) + \frac{\delta}{r} \quad (16)$$

where $G(r)$ is the conductance out of a sphere of radius r , $G(\infty)$ is a parameter describing the infinite-radius limit of the conductance, and δ describes the approach to the infinite size limit. Notably, the Tascini *et al.* simulations predict a positive δ , where smaller particles exhibit high interfacial thermal conductance and approach an infinite surface limit that has lower thermal conductance to the solvent. This makes intuitive sense – one might expect the large particle limit to approach the behavior of flat interfaces.

To test this hypothesis, we have computed heat transfer out of gold nanospheres that were in direct contact with a molecular solvent. The spheres were cut out of an infinite FCC lattice and spanned a range of sizes. Because of the cuts in the underlying lattice, the spheres expose many surface facets including patches of the (111), (100), and (110) facets. We have compared the interfacial thermal conductance out of the spheres with similarly-sized icosahedral particles that exhibit only (111) facets and cuboctahedral particles that display only (111) and (100) facets. We have also compared the interfacial thermal conductance to flat interfaces that match the facets exposed on the surfaces of the spheres.

One possible explanation for an empirical relationship like Eq. (16) is that there is a significant contribution to interfacial thermal conductance that depends on the surface area to volume ratio, suggesting a large role for the surface atoms. In our previous work, the thermal conductance out of chemically-modified gold surfaces was examined via reverse nonequilibrium molecular dynamics (RNEMD). [? ? ?] In these studies, surfactants attached to the gold surfaces contained a

strong gold – sulfur interaction that acted as a bridge for vibrational energy to travel to the ligand. Although the presence and density of the ligand layer has a large effect on the interfacial conductance, no clear trend was established regarding the size and curvature of the underlying nanoparticles. Previous studies from Tascini *et al.*[?] and Ong *et al.*[?] predict a decrease in the interfacial thermal conductance as the particle radius increases, although Ong *et al.*[?] and Zanjani *et al.*[?] predict higher thermal conductivity with increasing core diameter in nanocrystal arrays. However, if surface modifications dominate conductance, the presence of a moderate density of ligands will obscure the effects of particle curvature.

0.0.4.1 Size- and temperature-dependent particle morphologies

The nanoparticles simulated for this work ranged in size from 309 atoms to 14,993 atoms. Ercolessi *et al.*[?] annealed at temperatures from 400K to 1400K and found the dominant structures for different sizes of gold particles ($N = 100\text{--}900$ atoms). For $N = 100\text{--}200$, the structures were dominated by glassy clusters while for $N = 200\text{--}900$, the structures were predominantly cuboctahedral. Similarly, Myshlyavtsev and Stishenko found, when comparing gold nanostructures, a transition from a fully (111) icosahedral structure to a (100)-terminated cuboctahedral structures between 561 to 1,415 atoms, depending on the potential energy function.[?] Distinct vibrational densities of states have also been observed for the cuboctahedral clusters relative to icosahedra.[?]

In a study of the thermal stability of gold icosahedra, Wang *et al.*[?] found that softening of the vertex and edge atoms occurs at $\approx 800\text{K}$. During this process they saw enhanced surface atom diffusion due to the mobility of the vertex and

edge atoms.

The size range ($N = 300\text{-}15,000$) and temperatures (250K) for the calculations described here exhibit stable icosahedra with relatively low surface atom mobility, except for the smallest ($r < 15 \text{ \AA}$) particles, which may be metastable relative to cuboctahedra.

0.0.4.2 Theory

Under the diffuse mismatch model (DMM), the thermal conductance at an interface between a and b can be approximated,

$$G_{ab} = \frac{1}{4\pi} \sum_p \int_{\omega} \int_{\theta} \int_{\phi} \hbar\omega \frac{\partial f}{\partial T} v_a \rho_a \tau_{ab} \cos \theta \sin \theta d\theta d\phi d\omega \quad (17)$$

where f is the Bose-Einstein distribution function, $v_a(\omega, p)$ is the group velocity (on side a) for a phonon characterized by frequency ω , moving in direction (θ, ϕ) with polarization p . The relevant material properties are the density of phonon states, $\rho_a(\omega, p)$ and the transmission probability, $\tau_{ab}(\omega, p)$, at the interface.[? ? ?]

The diffuse mismatch model has a number of significant issues, particularly when the Debye model does a poor job representing the density of states, or where there is a fictitious boundary between identical materials (where the DMM predicts a non-zero resistance).[?] There is also an assumption of detailed balance built-in to the model,[?] which requires the two sides to be at equilibrium. This assumption is violated under non-equilibrium conditions, as in the RNEMD simulations used here. Although the DMM is not quantitative, it does suggest a role for frequency-dependent phonon transmission at the interface. It also suggests that isolating the frequencies of the phonons that are moving towards the interface

could aid in understanding interfacial conductance.

Using atomic velocities projected in a direction normal to the interface,

$$v_i^\perp(t) = \mathbf{v}_i(t) \cdot \hat{\mathbf{n}}, \quad (18)$$

it is straightforward to compute vibrational power spectra,

$$\rho^\perp(\omega) = \frac{1}{\tau} \int_{-\tau/2}^{\tau/2} \langle v^\perp(t) \cdot v^\perp(0) \rangle e^{-i\omega t} dt \quad (19)$$

which have been averaged over direction and polarization, where τ is the total observation time for the autocorrelation function. We can use this to approximate the density of phonon states of the two materials near the interface, which can provide a clearer picture of vibrational communication between the two materials. By further restricting the density of states calculation to specific atoms at the metallic side of the interface, we hope to provide a mechanism for heat flow from the solid and into the surrounding liquid.

To compute interfacial thermal conductance values directly, we rely on reverse non-equilibrium molecular dynamics (RNEMD) simulations.[? ?] RNEMD imposes an unphysical kinetic energy exchange between the center of the particle and a spherical shell of solvent that is well-separated from the interface. The system responds by creating a thermal gradient in the metal and solvent regions, and a temperature discontinuity at the interface between the particle and the solvent. The Kapitza resistance of the interface,

$$R_K = \frac{1}{G} = \frac{1}{q_r} \sum_i (T_{i+i} - T_i) 4\pi r_i^2, \quad (20)$$

is estimated by summing the individual thermal resistances of concentric spherical

shells as the radius increases.[?] Here, T_i is the temperature of a shell with radius r_i , and q_r is the heat rate (the relevant measure of thermal transport in spherical geometries). The heat rate is the surface area of the particle times that of the imposed flux. The interfacial thermal conductance of the interface, G is the inverse of the net Kapitza resistance. For interfaces of appreciable width, the relevant shells for measuring interfacial resistance are the largest shell that is unambiguously in the particle and the smallest shell that is unambiguously in the solvent.

For planar or periodic geometries, the interfacial thermal conductance can be similarly computed by imposing a non-physical flux between two separated slabs in the simulation cell. In this case, the Kapitza resistance,

$$R_K = \frac{1}{G} = \frac{\Delta T}{J_z}, \quad (21)$$

depends on the imposed kinetic energy flux, J_z , in a direction normal to the interface (z), and the steady-state temperature drop, ΔT , across the interface.[?]

0.0.5 Computational Details

Solvated gold nanoparticles ranging in diameter from 20-80 Å were simulated using reverse non-equilibrium molecular dynamics (RNEMD) in a spherical shell of hexane. Similar planar systems, displaying (111), (110), and (100) facets with hexane solvent were also prepared. The following sections describe the potentials used to calculate the interactions in the system as well as the simulation protocol.

0.0.5.1 Force Fields

For this work, gold – gold interactions are calculated using the quantum Sutton-Chen (QSC) model.[?] The hexane solvent is described by the TraPPE united atom (UA) model.[?] The bonds in TraPPE-UA are rigid, but here the bonds are made flexible using harmonic force constants borrowed from OPLS-AA for intra-molecular sites closer than 3 bonds.[?] The interactions between Au atoms and atoms on the hexane molecules were fit to a pairwise Lennard-Jones potentials based on a study by Hautman and Klein for Au(111) surfaces.[?] Details of the interaction potentials are identical to previous work on heat transport for thiolate-protected gold nanospheres.[?]

0.0.5.2 Simulation Protocol

The gold nanospheres were prepared in the same fashion as in Stocker *et al.*[?] Icosahedral particles were constructed in nested shell structures, built around an ideal icosahedral core. Cuboctahedral particles were built by cutting (111) and (100) facets from a FCC lattice. Both icosahedral and cuboctahedral particles were thermally equilibrated before being solvated in the same manner as the spheres. Once solvated, the systems were equilibrated for a minimum of 1 ns using the Langevin Hull integrator with an external bath characterized by 50 atm of pressure and a temperature bath at 250K.[?]

Planar interfaces displaying the Au(111), Au(110), and Au(100) facets were prepared as slabs $\sim 20 \text{ \AA}$ thick with the relevant facets rotated normal to the z -axis. Surface stress was removed by relaxing the systems for 1 ns at 250 K in a constant surface tension ($N\gamma T$) ensemble with zero applied surface tension, followed by 1 ns in the microcanonical (NVE) ensemble. Hexane molecules were

packed into the remaining box volume with a density of 0.6548 g/cm³. The solvated systems were then equilibrated using the canonical (NVT) ensemble at 250 K for 1 ns followed by further relaxation in the microcanonical ensemble for 1 ns.

Following equilibration, the relevant thermal flux was applied for 1 ns for the nanoparticle systems and 3 ns for the planar systems, allowing for a steady-state temperature gradients to develop. Mean temperatures of the system remained at 250K, preserving the solvent cluster around the nanoparticles and preventing the formation of a vapor layer. Thermal coupling to the external temperature bath was removed to avoid interference with the imposed flux. The metal particles equilibrated rapidly, and were typically found with elevated temperatures (\sim 300K) relative to the bulk. Because the solvent volume is large relative to the particles, the solvent finds a steady state temperature just below 250K throughout most of the volume. Adjacent to the surface of the particles, solvent temperatures are typically close to 260K. The TraPPE-UA hexane model boils at \sim 330K, so the simulation conditions are reasonable for maintaining liquid surroundings for the particles. All simulations were carried out with the open source molecular dynamics package, OpenMD.[? ?]

Five separate configurations for each system size were simulated to provide statistical independence of the hexane packing. Thermal conductance was calculated using the same methods found in Stocker *et al.*[?] for the non-periodic systems and for the planar systems.[?]

0.0.6 Results and Discussion

The interfacial thermal conductance (G) for hexane-solvated spherical, icosahedral, and cuboctahedral Au nanoparticles was computed using RNEMD sim-

ulations, and was compared with the same quantity for a series of planar gold interfaces, including the Au(111), Au(100), and Au(110) interfaces. These surfaces are all exhibited as microfacets on the surfaces of the nanospheres, and the Au(111) facet is the primary facet displayed by the icosahedra.

Computed interfacial thermal conductance values for the icosahedra, cuboctahedra, nanospheres, and flat facets are shown in Fig. 12. The nanospheres have a pronounced dependence on the particle radius, r , while the icosahedral conductance stays relatively close to the value obtained for the Au(110) facet. Thermal transport out of the cuboctahedral particles show a mostly linear dependence on particle radius. The smooth line going through the conductance values for the spheres is a fit using the Tascini *et al.*[?] model (Eq. (16)) with $G(\infty) = 49.25 \text{ MW m}^{-2} \text{ K}^{-1}$, and $\delta = -156.25 \text{ MW \AA m}^{-2} \text{ K}^{-1}$. Notably, our simulations project a value for the interfacial conductance of the infinite spheres that is significantly *higher* than many of the flat facets. To explain this observation, we discuss the surface density of undercoordinated atoms and the vibrational densities of states of these undercoordinated atoms the following sections.

The spherical particles display all three of the planar facets (as well as small regions of higher index facets), and for most of the size range simulated, they also exhibit a significantly higher interfacial thermal conductance than the low-index facets.

For icosahedral particles, there is no clear dependence of G on the particle size, and the larger particles exhibit thermal conductance values slightly above the expected (111) conductance for particles with $r \approx 35 \text{ \AA}$. There is some instability in the values of G in the range of $r = 18 - 22 \text{ \AA}$, which is near the 15 \AA transition from stable icosahedra to cuboctahedra.[?]

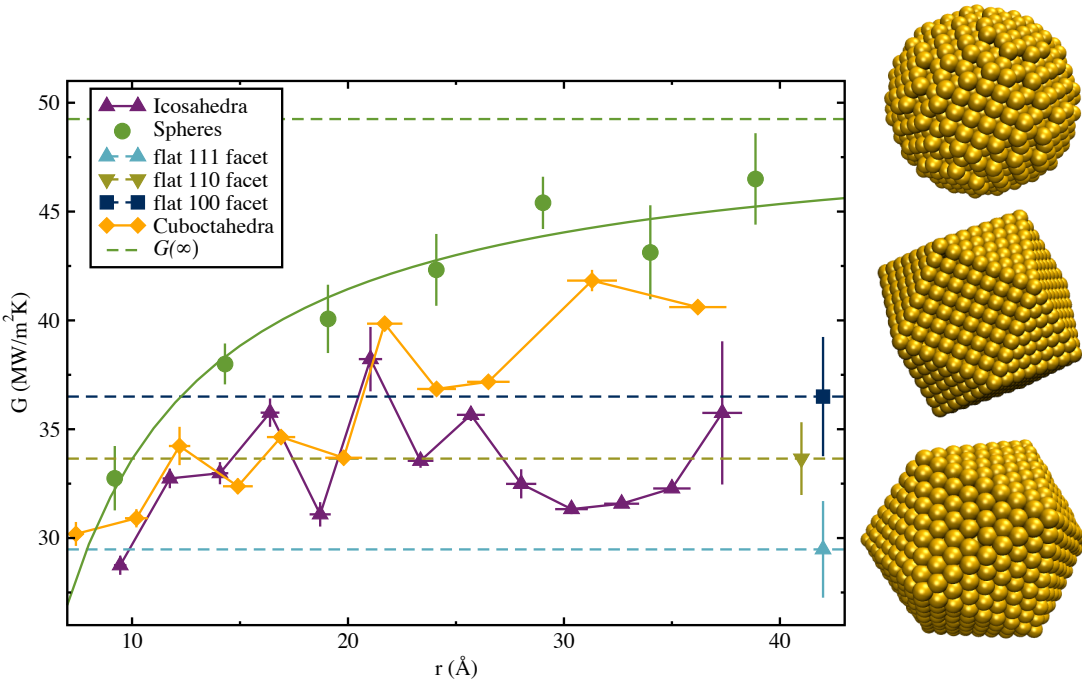


Figure 12. Interfacial thermal conductance, G , for bare gold nanospheres, cuboctahedra, and icosahedra in contact with hexane solvent. Conductances for flat Au(111), Au(100), and Au(110) interfaces are indicated with dashed horizontal lines. A fit using the model of Tascini *et al.* is shown along with the predicted value of $G(\infty)$, the infinite particle limit.

0.0.6.1 Surface Atom Undercoordination

For the three flat facets, the primary feature that differentiates the facets is the coordination number (CN) of the atoms that are exposed to the solvent. In bulk Au, the coordination number of the atoms is 12; six neighbors in plane, three below the atom, and three above the atom. Any atom with a coordination number below 12 would exhibit more vibrational freedom and is considered an undercoordinated site. The Au(111) surface presents gold atoms with nine surrounding metallic atoms ($CN = 9$) to the solvent, while the Au(100) facet surface exposes atoms with $CN = 8$. Au(110) displays a corrugated surface where the two outer layers of atoms have $CN = 7$ and $CN = 11$, respectively (see Fig. S1 in the Supporting Information). Both of these coordination environments approach the surface close enough to interact with the solvent atoms (see Fig. S6 in the SI).

Reducing the number of metallic interactions allows the surface atoms to vibrate at different frequencies than the interior atoms, populating a portion of the spectrum that overlaps with collective motions of the solvent molecules. This mechanism may explain the enhanced interfacial thermal conductance of the (100) facet relative to the (111) facet. However, it does not explain why the (110) facet displays an intermediate conductance even though the surface atoms have a lower coordination number than the (100) facet. To answer this question, it is important to consider the surface density of the undercoordinated atoms as well as the vibrational freedom allowed by the undercoordination. In Table 1 we show the density of the solvent-accessible undercoordinated surface atoms for the three facets. Although the (110) facet displays 7- and 11-coordinated atoms to the solvent, the $CN = 11$ have vibrational dynamics that are essentially equivalent to the bulk gold (Fig. S3 in the SI), and the surface density of these atoms is significantly

lower than the surface density displayed by the (111) and (100) facets.

TABLE 1

The density of undercoordinated gold atoms at the surface of a facet.

Facet	CN	Surface Density (atoms Å ⁻²)
(111)	9	0.1394
(100)	8	0.1214
(110)	7	0.0877
	11	0.0877

It is therefore likely that not only the undercoordination of surface atoms, but also the density of these undercoordinated atoms plays a role in thermal conductance. In the nanoparticles, surface atoms that are in physical contact with the solvent have a range of coordination numbers from 5 – 9, but only CN = 6 – 9 appear with high probability. The surface coordination densities have been calculated for all of our samples, and the undercoordination density is distinct for the spheres, icosahedra, and cuboctahedra (See Fig. 13).

The icosahedral particles display three coordination environments: the vertices have a CN = 6, while the triangular (111) faces of the particle have a CN = 9,

and the edges connecting the faces have CN = 8. As the radius of the icosahedral particles increases, the surface is dominated by the triangular facets, so the surface density of the CN = 9 rises. For perfect icosahedra, the ideal surface densities are shown as dashed lines in Fig. 13.

For the simulated systems at 250K, surface vibrational motion leads to coordination numbers that are lower than one would expect for an ideal icosahedron. This is evident in the populations of the CN = 9, which is 20–50% lower than the ideal case.

In the spherical particles, the surface density of undercoordinated atoms stabilizes above $r = 25$ Å. However, the densities of the undercoordinated atoms never approach any of the flat facet values (as is the case in the icosahedra). We may estimate the large radius limit of the spheres by averaging the surface densities for ideal spheres of radii 95–100 Å. These are shown with open symbols in the upper panel of Fig. 13.

The cuboctahedral particles approach the ideal solid surface densities as the radius of the particle increases. Beyond a radius of 15 Å the cuboctahedra are no longer dominated by edge atoms and flat facets form the majority of the surface. After this transition the surface densities quickly stabilize to nearly-ideal cuboctahedral structures.

Calculations of the population densities of under-coordinated surface atoms for ideal geometries are given in the Supporting Information.

0.0.6.2 Phonon Spectra

By selecting specific groups of atoms while computing the vibrational power spectrum (Eq. 19) we can explore the role of undercoordination on surface vibra-

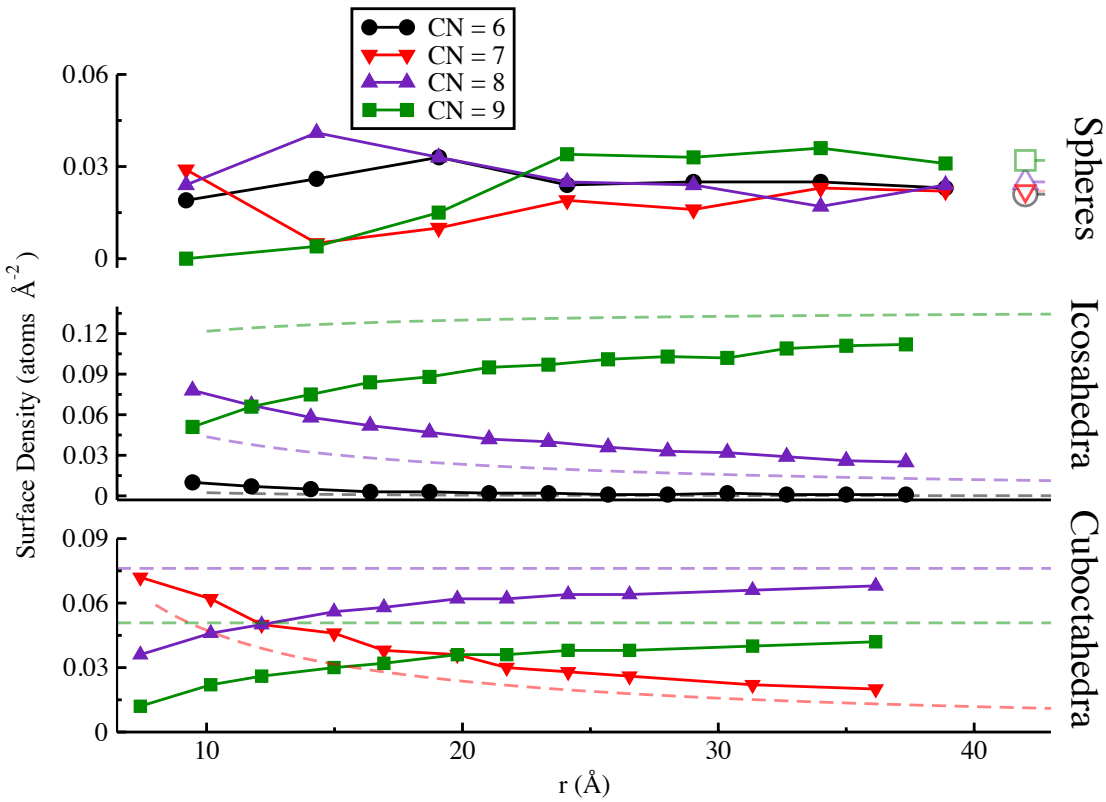


Figure 13. The coordination number of surface atoms as a function of particle size. Filled data points are sampled from simulations, while the dashed lines correspond to ideal icosahedral and cuboctahedral solids. In the spherical case, the large radius limits are shown with open symbols. The large radius limit for the spheres approaches a constant density for all undercoordinated sites, while for the icosahedra, the 9-coordinated (111) facet dominates. In larger cuboctahedra, the relative fraction of 8- and 9-coordinated surface atoms is largely independent of particle size.

tional motion. For thermal transport, the regions of interest are the nanoparticle atoms in direct physical contact with the solvent, and those solvent molecules that form the first solvation shell, i.e. $< 5\text{\AA}$ from the gold surface.

Under the QSC potential, the bulk gold vibrational power spectrum displays two broad peaks, one at $\sim 60 - 80 \text{ cm}^{-1}$, and another sharper peak at $\sim 125 \text{ cm}^{-1}$. The vibrational densities of states for the four outer layers of the nanoparticles are shown in Fig. 14. The surface layers for all particles are dominated by the low frequency portion of the spectrum ($< 70 \text{ cm}^{-1}$) and display small morphology-dependent features at higher frequencies (140 cm^{-1}). The low-frequency peak appears at significantly lower frequencies than in the bulk, and the higher frequency contribution is significantly broadened. Spheres and cuboctahedra recover bulk-like densities of states relatively close to the surface – only the surface and second shell are significantly altered from the bulk gold density of states. In the spheres, the higher frequency contribution ($\sim 150 \text{ cm}^{-1}$) resembles the vibrational density of states for undercoordinated atoms with CN=8 or 7 (see Supporting Information).

The icosahedra still have perturbed spectra even four layers into the particles. Icosahedral particles grow around a core with I_h symmetry, and the local environment around the atoms deviates significantly from perfect FCC ordering. The local bond orientational order can be described using the method of Steinhardt *et al.*[?] Plots of the radial fraction of FCC ordering for all particles are shown in the Supporting Information, and they show substantial loss of FCC ordering in icosahedral particles. The icosahedra therefore display phonon spectra that are enhanced in the higher frequency peaks ($\sim 130 \text{ cm}^{-1}$) at the expense of the broad $\sim 60 - 80 \text{ cm}^{-1}$ feature.

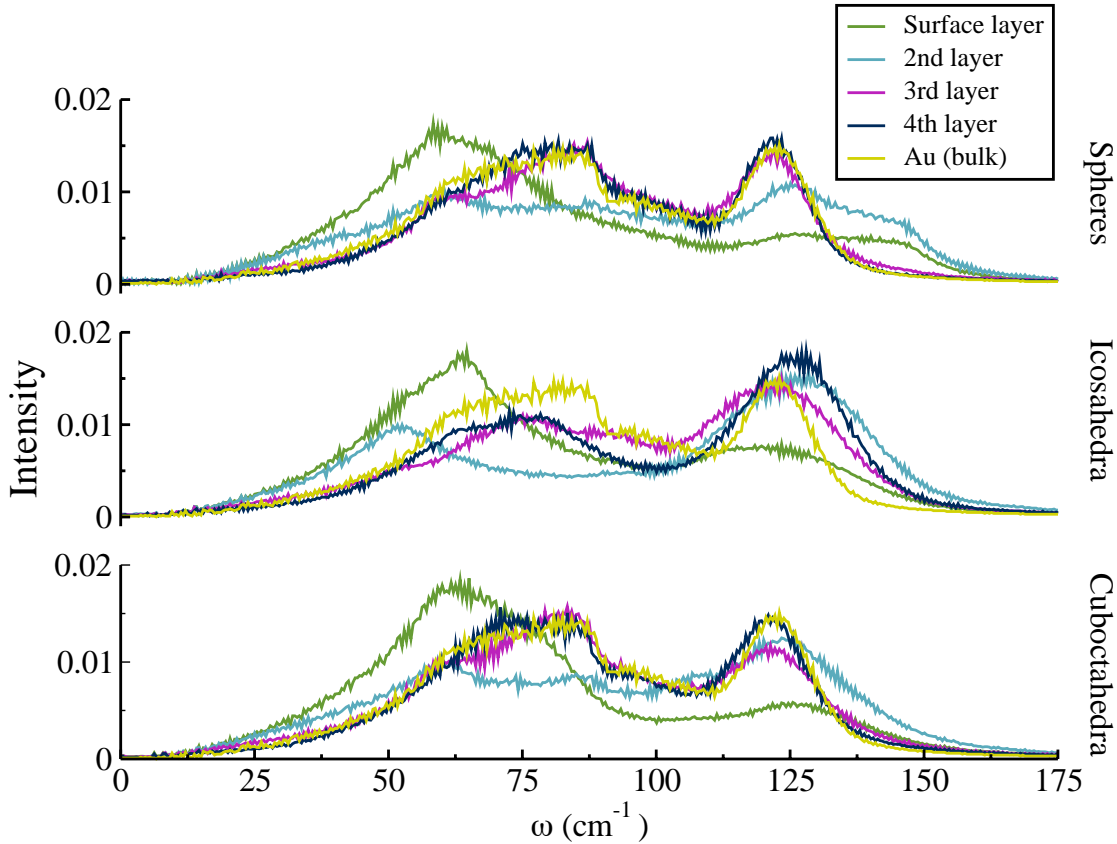


Figure 14. The projected vibrational density of states (Eq. 19) for individual layers in the largest gold nanoparticles (top: spheres, middle: icosahedra, bottom: cuboctahedra). In all systems, the surface layer (green) is significantly enhanced at low frequencies and is shifted down by $\sim 20 \text{ cm}^{-1}$. The Au (bulk) curve shown for comparison is from a perfect FCC lattice in periodic boundary conditions.

Comparison of the vibrational density of states of all the gold atoms displays some important differences between the icosahedral structures and the FCC-based spheres and cuboctahedra (Fig. 15). Icosahedral particles have non-FCC ordering deep into the particle, and this manifests as a shift in phonon population from the broad low-frequency region to the higher frequency peak, even for the largest of the particles that were studied. For comparison, the largest spheres and icosahedra have only slight differences in their “bulk” phonon density of states.

At the surfaces of the particles, the differences are nearly all in the higher frequency portion of the spectrum ($> 100\text{cm}^{-1}$), indicating that the surface undercoordination primarily alters high-frequency transmission into the solvent. This suggests roles for bulk crystalline ordering as well as surface undercoordination in any model for the interfacial thermal conductance.

Except in the case of the icosahedra, vibrational power spectra that include all gold atoms in the nanoparticles do not show significant dependence on particle radius (see Supporting Information). This suggests that mismatch models (like AMM or DMM) that use only bulk properties will not be able to capture the surface behavior that is relevant to heat transfer at the nanoscale.

Solvent vibrational densities of states are remarkably similar for the icosahedral and spherical particles, even for solvent that is within 5 Å of the interface (See Supporting Information). Therefore, we propose that any model for interfacial thermal transport in these systems would need to include the lattice structure of the particle and the quantity and solvent accessibility of specific kinds of undercoordinated metal atoms.

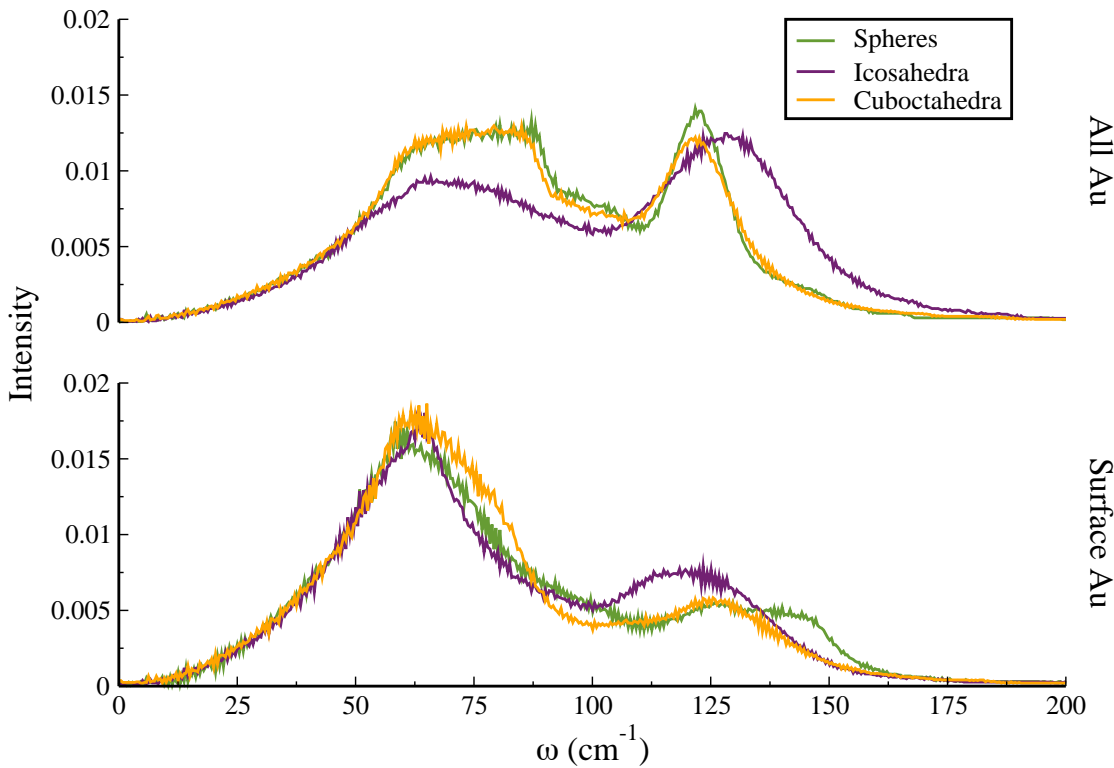


Figure 15. The projected vibrational density of states for all gold atoms (top panel) shows that the phonons in FCC-like nanoparticles (spheres, cuboctahedra) have similar frequency representation, while the non-FCC structures (icosahedra) have significantly altered “bulk” spectra. For surface atoms (bottom panel), the differences in surface undercoordination appear at higher frequencies. These spectra were computed for the largest particles in each of the different morphologies.

0.0.6.3 A Simple Model for Bare Nanoparticle Conductance

The vibrational densities of states suggest the bare metallic nanoparticles exhibit different bulk phonon frequencies that depend on crystalline packing, and different surface spectra that depend on surface undercoordination. Both of the bulk and surface frequencies can effect thermal transport, so we provide a simple model in terms of a linear combination of surface densities of undercoordinated atoms,

$$G \approx a \text{ CN}_6 + b \text{ CN}_7 + c (1 + c' \delta_{\text{ico}}) \text{ CN}_8 + d (1 + d' \delta_{\text{ico}}) \text{ CN}_9 \quad (22)$$

where, $a - d$ are coordination transport coefficients with the units of 10^{-20} MW/K and CN_n have surface density units ($1/\text{\AA}^2$) for surface atoms with coordination number n . The delta function, δ_{ico} is set to unity for icosahedral structures, and zero for FCC-like nanoparticles. The coefficients c' and d' are weighting factors that recognize the differences in the bulk density of states in the icosahedral particles. Fitting the six parameters was done using a simple ordinary least squares model with data from all simulated particles.

With Eq. (22) it should be possible to predict the interfacial thermal conductance for bare gold nanoparticles in hexane based only on a structural analysis of the surface for coordination densities and the interior of the particle for crystalline structure. The predicted (and simulated) values of the thermal conductance are given in Fig. 16. With a coefficient of determination (R^2) value of 0.656, this fit does not predict G with a high degree of certainty, but it does suggest the large role that undercoordinated surface atoms play in conductance. Coefficients used in Eq. (22) are given in the supporting information.

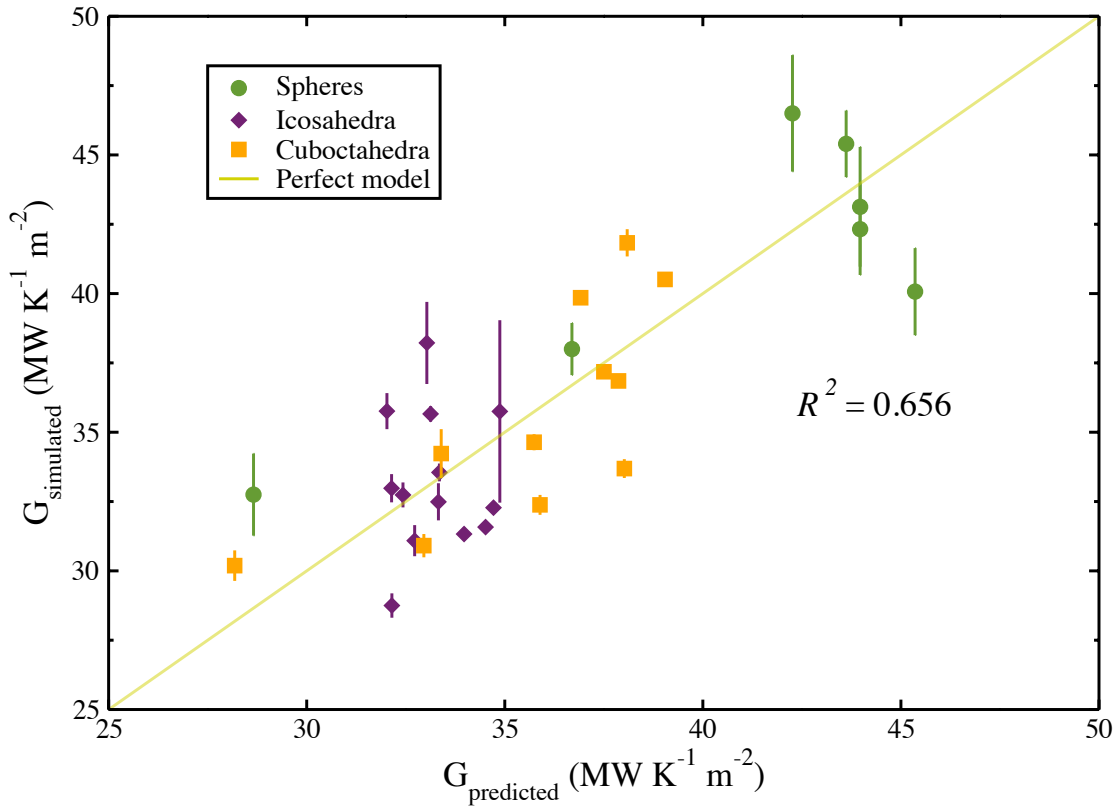


Figure 16. Structurally-predicted thermal conductance values from Eq. (22) compared with the simulated thermal conductance values. Error bars indicate the standard error computed using five replica simulations.

0.0.7 Conclusions

The primary observation of this work is that particle morphology has a significant effect on interfacial thermal conductance from bare particles to the surrounding solvent. In particular, spherical and cuboctahedra particles have a size-dependent interfacial thermal conductance, while icosahedral particles conduct heat to the surrounding solvent only slightly better than the flat (111) facets.

We have explored one explanation for this difference in terms of the density of undercoordinated sites on the surfaces of these three particle morphologies. Nanospheres, because they are carved out of an underlying FCC lattice, expose significantly undercoordinated atoms ($CN = 6 - 8$) to the solvent. For very small spheres, microfacets of (111), (100), and (110) dominate the surface, but for larger particles, the density of undercoordinated atoms becomes a significant fraction of the exposed atoms. In large icosahedral particles, the particles are dominated by (111) faces, and the $CN = 9$ atoms dominate the surface. Similarly, in large cuboctahedral particles, the (111) and (100) facets are both present, and the $CN = 9$ and $CN = 8$ atoms share the particle surface in a 2:3 ratio. Surface atom undercoordination leads directly to changes in the surface vibrational density of states, particularly at frequencies around $\sim 150\text{ cm}^{-1}$. The linear model suggests that differences in surface atom undercoordination (particularly for atoms that are undercoordinated relative to a flat facet) may be largely responsible for our observations.

This is not a complete explanation for the conductance values, however, as the large icosahedral particles exhibit G values above the planar (111) facet, and large cuboctahedra have G values above *both* the (111) and (100) facets. Edge and vertex atoms in these clusters may play an outsized role, and collective low-

frequency modes of the particles may also be important, as the underlying “bulk” density of states also depends on particle morphology.

*This document was prepared & typeset with pdfL^AT_EX, and formattted with
NDDiss2_ε classfile (v3.0[2005/07/27]) provided by Sameer Vijay.*